CHALMERS
UNIVERSITY OF TECHNOLOGY

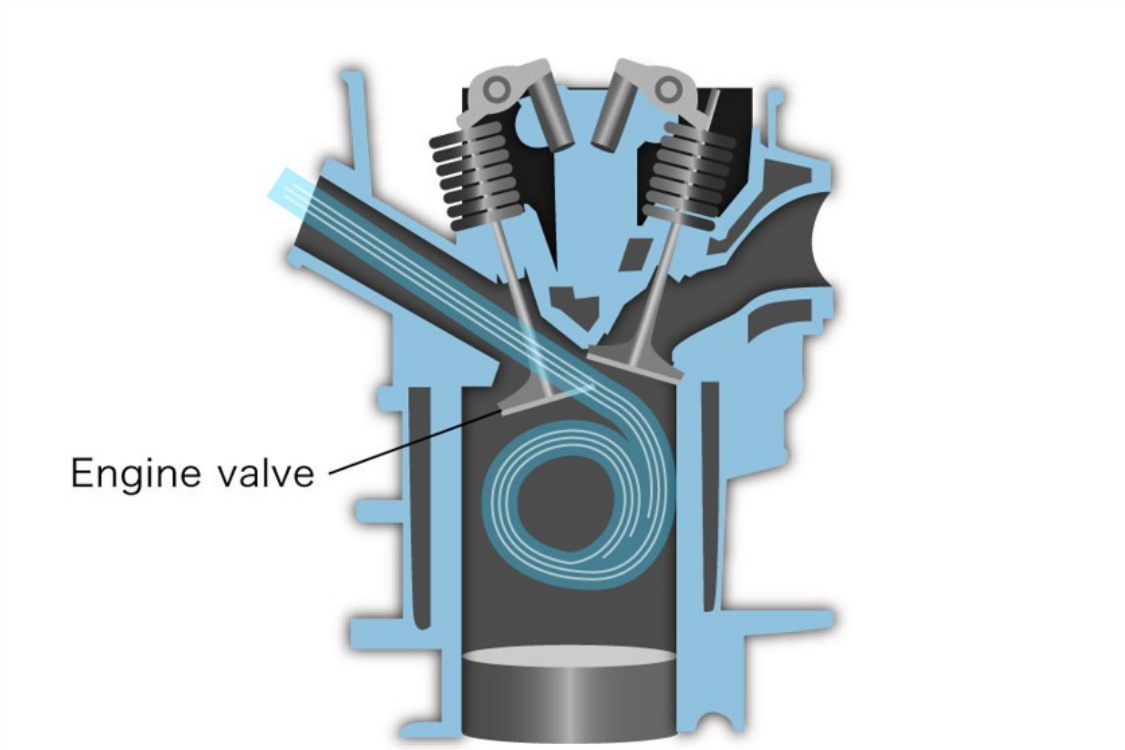

Environmentally Friendly Nitriding for Valves in Hydrogen Internal Combustion Engine

Master's thesis in Materials Engineering

SUBI YUSHANJIANG

DEPARTMENT OF INDUSTRIAL AND MATERIALS SCIENCE
CHALMERS UNIVERSITY OF TECHNOLOGY
Gothenburg, Sweden 2026
www.chalmers.se

Master's thesis 2026

Environmentally Friendly Nitriding for Valves in Hydrogen Internal Combustion Engine

SUBI YUSHANJIANG



CHALMERS
UNIVERSITY OF TECHNOLOGY

Department of Industrial and Materials Science
Materials and Manufacture
Chalmers University of Technology
Gothenburg, Sweden 2026

Environmentally Friendly Nitriding for Valves in Hydrogen Internal Combustion Engine

SUBI YUSHANJIANG

© SUBI YUSHANJIANG, 2026.

Supervisor: Bala Malladi, Emmy Yu Cao, Materials and Manufacturing
Examiner: Emmy Yu Cao, Materials and Manufacturing

Master's Thesis 2026
Department of Industrial and Materials Science
Division of Materials and Manufacture
Chalmers University of Technology
SE-412 96 Gothenburg
Telephone +46 31 772 1000

Cover: Cross-sectional illustration of a hydrogen internal combustion engine, highlighting the position of the engine valve.[1]

Typeset in LaTeX
Printed by Chalmers Reproservice
Gothenburg, Sweden 2026

Environmentally Friendly Nitriding for Valves in Hydrogen
Internal Combustion Engine
SUBI YUSHANJIANG
Department of Mechanical Engineering
Chalmers University of Technology

Abstract

Hydrogen-fueled internal combustion engines (ICEs) represent a promising next-generation propulsion technology. Engine valves are critical components that require high strength and wear resistance, properties commonly enhanced through surface hardening/nitriding. Conventional hard chromium (Cr^{6+}) coatings are increasingly being phased out due to environmental and health concerns associated with the (Cr^{6+}) containing electroplating process. This thesis investigates environmentally friendly nitriding technologies as alternatives for engine valves used in hydrogen-fueled ICEs developed by TRATON Group R&D. Gas nitriding and plasma nitriding were applied to two valve materials: the austenitic 3015 alloy and the martensitic X45CrSi9-3 steel, both used for valve stems.

The study combined optical microscopy, SEM, EBSD, microhardness testing, hydrogen content analysis, slow strain rate tensile testing, and fracture surface analysis. As-received valves were examined first to evaluate the differences in nitriding layer forms by gas nitriding and plasma nitriding. The influence of the nitriding layer on microstructure and hydrogen uptake was studied. Subsequently, the tensile test samples extracted from the valve were sent to Bodycote for re-nitriding by a gaseous method. Hydrogen was then introduced electrochemically to the samples with and without nitriding. The influence of gas nitriding on mechanical behavior was further investigated and compared.

The results showed that nitrided surface layers were formed in both nitriding processes, but the layer thickness and uniformity depended on both the substrate material and the nitriding process. Gas nitriding generally produced a thicker layer, while plasma nitriding gave a thinner and more geometry-dependent layer. Hydrogen analysis indicated that 3015 retained more hydrogen than X45CrSi9-3, and hydrogen uptake caused a pronounced loss of ductility, especially in X45CrSi9-3. Fractography showed that nitrided specimens developed thinner hydrogen-affected brittle zones than unnitrided specimens, suggesting that nitriding can help restrict hydrogen-assisted fracture. However, the re-nitrided tensile specimens also showed that an overly thick or uneven nitrided layer can reduce plasticity even without hydrogen uptake, highlighting the need for process optimization.

Overall, the thesis shows that nitriding may improve the surface performance of engine valves for hydrogen applications, but the treatment window must be carefully controlled to balance hardness, layer thickness, and resistance to hydrogen embrittlement.

Keywords: 3015 Alloy, X45CrSi9-3 steel, Engine valve, Plasma Nitriding, Gas Nitriding, Electrochemical Charging, TDS, Hydrogen Embrittlement.

Acknowledgements

I would like to express my sincere gratitude to everyone who has supported and guided me throughout the thesis project. This work would not have been possible without the encouragement, insights, and contributions of many individuals.
First and foremost, I am deeply thankful to my examiner and teacher, Professor Emmy Cao. In the beginning, she gave me the opportunity to work as a research assistant on the Area of Advanced (AoA) project, focusing on hydrogen embrittlement, and this semester gave me the chance to continue my master's thesis in the same field. With her kind mentorship, I am more familiar with the topic and have increased my passion for research.
I would also like to thank my supervisor, Bala Malladi, for his expertise, encouragement, and support during the project. During the last two months of my master's thesis, Bala, although he was no longer working at Chalmers and was not my supervisor, still continued to help me and answer my questions. Big thanks for his responsibility, and best wishes for his future career and life.
Many individuals at Chalmers University of Technology provided assistance for this project. I would like to extend my thanks to Vishnu Anilkumar for guiding and conducting SEM characterization for me during the project, to Antonio Mulone for training me on various equipment, such as sample preparation, SEM, EBSD, and tensile testing, to Eic Tam for support in the chemical lab, Yao Shi for academic discussion, and to Anders Bragee for preparing the samples.
Additional thanks to the Engineer of Sweden's Environmental Fund and Sweden Bank for providing a master's thesis scholarship for this project.
I would like to thank Bodycote for helping me conduct gas nitriding for my specimen. Special thanks to Fredrik Lundin and Ghorbani Arvin for their support. I would also like to thank TRATON Group R&D for providing samples and project support. Special thanks to Åsa Gustafsson, Peter Skoglund, Peter Scharf and Lars Jacobsson for their helpful discussion.
Last and most importantly, I would like to express my deepest gratitude and love to my wife, Nargiza, and my family for their unselfish support and help.

SUBI YUSHANJIANG, Gothenburg, June 2026

List of Acronyms

Below is the list of acronyms that have been used throughout this thesis listed in alphabetical order:

AIDE	Adsorption-Induced Dislocation Emission
BCC	Body-centered cubic
EBSD	Electron Backscatter Diffraction
EDM	Electrical Discharge Machining
EDS	Energy-Dispersive X-ray Spectroscopy
FCC	Face-centered cubic
HE	Hydrogen Embrittlement
HEI	Hydrogen Embrittlement Index
HELP	Hydrogen-Enhanced Localized Plasticity Mechanism
HEDE	Hydrogen-Enhanced Decohesion Mechanism
IPF	Inverse pole figure
MS	Mass Spectrometry
OPS	oxide polishing suspension
OM	Optical Microscopy
SEM	Scanning Electron Microscopy
SSRT	Slow strain rate tensile
TEM	Transmission Electron Microscopy
TDS	Thermal Desorption Spectroscopy
TCD	thermal conductivity detector

Nomenclature

Below is the nomenclature of indices, sets, parameters, and variables that have been used throughout this thesis.

Parameters

δ_L	Hydrogen embrittlement index
δ_0	Total elongation of the uncharged sample
δ_H	Total elongation of the hydrogen charged sample
X_α	thickness of the nitrided layer
t	time
D	diffusion coefficient
ε-nitride	Epsilon iron nitride, $Fe_{2-3}N$
γ'-nitride	Gamma-prime iron nitride, Fe_4N
H_{ad}	Adsorbed hydrogen
H_{ab}	Absorbed hydrogen
M	Metal
J	Diffusion flux
$\frac{\partial C}{\partial x}$	Hydrogen concentration gradient
$\frac{\partial C}{\partial t}$	Changes in Hydrogen concentration over time
Q	activation energy
T	Temperature
γ	Austenite phase
α	Ferrite phase
E_b	Hydrogen trap activation energy
R_m	Ultimate tensile strength
$R_{p0.2}$	Yield strength
δ	Elongation

φ	Reduction of area

Contents

List of Acronyms **ix**

Nomenclature **xi**

List of Figures **xv**

List of Tables **xix**

1 Introduction **1**

2 Engine Valve **3**
2.1 3015 Alloy 4
2.2 X45CrSi9-3 steel 5
2.3 Nitriding Process 6
2.3.1 Gas Nitriding Process 6
2.3.1.1 Mechanism of Gas Nitriding 6
2.3.1.2 Parameters of Gas Nitriding Process 7
2.3.2 Plasma Nitriding Process 8
2.3.2.1 Mechanism of Plasma Nitriding 8

3 Hydrogen Embrittlement **11**
3.1 Hydrogen Uptake 11
3.2 Hydrogen Solubility and Diffusion 12
3.3 Mechanism of Hydrogen Embrittlement 14
3.3.1 Hydrogen Pressure Theory 14
3.3.2 Hydrogen-Enhanced Localized Plasticity Mechanism (HELP) . 15
3.3.3 Hydrogen-Enhanced Decohesion Mechanism (HEDE) 15
3.3.4 Adsorption-Induced Dislocation Emission (AIDE) 16

4 Methods **19**
4.1 Sample Preparation 19
4.1.1 Metallographic Specimen 19
4.1.2 Tensile Test Specimen 19
4.1.3 Nitrided Specimen 20
4.2 Cathodic Hydrogen Charging 20
4.3 Characterization Techniques 21
4.3.1 Optical Microscopy (OM) 21

4.3.2 Scanning Electron Microscopy (SEM) . . . 21
4.3.3 Electron Backscatter Diffraction (EBSD) . . . 22
4.3.4 Hydrogen Measurement . . . 23
4.4 Mechanical Testing . . . 24
4.4.1 Hardness Test . . . 24
4.4.2 Slow Strain Rate Tensile Test . . . 24

5 Results and Discussion **25**
5.1 Microstructure . . . 25
5.1.1 As-Received Engine Valve . . . 25
5.1.2 Re-Nitrided Samples by Gas Nitriding in Bodycote . . . 30
5.2 Hydrogen Content analysis . . . 32
5.2.1 As-Received Engine Valve Materials . . . 32
5.2.2 Hydrogen Charged Engine Valve Materials . . . 34
5.3 Mechanical Properties . . . 35
5.3.1 Tensile Stress-Strain Responses . . . 35
5.3.1.1 X45CrSi9-3 Steel in the Valve Stem . . . 35
5.3.1.2 3015 Alloy in the Valve Stem . . . 37
5.3.2 Fractography . . . 39

6 Conclusions **45**

7 Future plan **47**

Bibliography **49**

List of Figures

2.1 Schematic illustration of the engine valve showing the different regions and materials. The red dashed line indicates the friction-welded joint between X45CrSi9-3 and 3015, while the blue dashed line indicates the boundary between the valve stem and valve head. 3
2.2 IPF map (A) and phase map (B) of 3015 austenitic alloy from the valve stem. 4
2.3 EDS element map of 3015 alloy 5
2.4 IPF map (A) and phase map (B) of X45CrSi9-3 martensitic steel . . 5
2.5 Schematic illustration of the gas nitriding process 7

3.1 Schematic of hydrogen traps in steel:(a) interstitial sites; (b) surface traps; (c) subsurface traps; (d) grain boundary traps; (e) dislocation traps; (f) vacancy traps [23] 12
3.2 Hydrogen solubility in pure iron as a function of temperature. (Hydrogen (H) contents expressed in wt%) [24] 14
3.3 Schematic of HELP mechanism [23] 15
3.4 Schematic diagrams illustrating the HEDE mechanism, showing tensile separation of atoms caused by hydrogen-induced weakening of interatomic bonds by (a) hydrogen in the lattice, (b) hydrogen adsorbed at crack tips, and (c) hydrogen at particle–matrix interfaces. [31] 16
3.5 Schematic diagram illustrating the adsorption-induced dislocation emission (AIDE) mechanism [36] 17

4.1 Geometry of tensile test specimen 19
4.2 Schematic illustration of an electrochemical hydrogen charging setup 20
4.3 Diagram of a compound microscope [37] 21
4.4 Schematic diagram showing the SEM interaction volume with dimensions. [38] 22
4.5 Schematic experimental set-up for EBSD collection. [39] 23

5.1 Schematic illustration of the engine valve materials and regions. Blue and red boxes indicate sampling locations for microstructural analysis of 3015 and X45CrSi9-3, respectively. 26
5.2 Microstructure of gas nitrided engine valve:(A) 3015 alloy, (B) X45CrSi9-3 26

5.3 Microstructure of plasma nitrided engine valve:(A) 3015 alloy, (B) X45CrSi9-3 26
5.4 Vickers microhardness profiles as a function of distance from the surface for Plasma Nitrided (PN) and Gas Nitrided (GN) treated X45CrSi9-3 and 3015 steels. 28
5.5 EDS line scan across the nitrided layer of GN and PN treated steels. (A) Gas nitrided 3015 alloy, (B) Gas nitrided X45CrSi9-3 steel, (C) Plasma nitrided 3015 alloy, (D) Plasma nitrided X45CrSi9-3 steel. . 29
5.6 Microstructure of valve head after gas and plasma nitriding. Schematic imaging locations are given in (A) for the valve face and (B) for the valve bottom. (C, D) Gas nitrided valve face and bottom; (E, F) Plasma nitrided valve face and bottom. 30
5.7 Microstructure and hardness profile of gas nitrided X45CrSi9-3: (A) Schematic of the tensile-test specimen, showing the cutting location (red dashed line) and vickers hardness test locations (red dots); (B) Vickers microhardness profile (HV0.1) for nitrided (red) and unnitrided (blue) steels from the grip section of the tensile specimen; (C) LOM image for right surface in A, (D) LOM image for top surface in A, (E) LOM image for left surface in A 31
5.8 Microstructure and hardness profile of gas nitrided 3015 alloy: (A) Schematic of the tensile-test specimen, showing the cutting location (red dashed line) and Vickers hardness test locations (red dots); (B) Vickers microhardness profile (HV0.01) for all surfaces of the nitrided steel from grip section of tensile specimen; (C) LOM image for right surface in A; (D) LOM image for Top surface in A; (E) LOM image for left surface in A; (f) LOM image for bottom surface in A. 32
5.9 (A) Total hydrogen content for 3015 alloy and X45CrSi9-3 steel under uncharged conditions. (B) Thermal desorption curve obtained based on carrier gas hot extraction for gas nitrided 3015 alloy under uncharged conditions. 33
5.10 Hydrogen content obtained by carrier gas hot extraction for plasma nitrided 3015 alloy (A) and X45CrSi9-3 steel (B), charged in 0.5 M H_2SO_4 + 3 g/L NH_4SCN electrolyte. 34
5.11 Tensile curves of as-received X45CrSi9-3 at different conditions of electrochemical hydrogen charging 35
5.12 Tensile curves of X45CrSi9-3 re-nitrided in Bodycote without hydrogen charging 36
5.13 Tensile curves of unnitrided 3015 alloy. (A) Uncharged samples, (B) Comparison of charged and uncharged samples 37
5.14 Tensile curves of the 3015 alloy re-nitrided in Bodycote 38
5.15 SEM images of the fracture surfaces of hydrogen-free tensile specimens: (A) Gas nitrided X45CrSi9-3, (B) Gas nitrided 3015, (C) Unnitrided X45CrSi9-3, (D) Unnitrided 3015. 40
5.16 Magnified images from the fracture surfaces in Fig.5.15. (A′) region A′ in Fig.5.15, (B′) region B′ in Fig.5.15, (C′) region C′ in Fig.5.15, (D′) region D′ in Fig.5.15. 41

5.17 SEM images of the fracture surfaces after SSRT from the nitrided (A-D) and unnitrided (E-H) 3015 alloys, charged at50 $°C$ and 15mA/cm^2 current density in 0.01M H_2SO_4 + 3g/L NH_4SCN electrolyte for 48h prior to tensile tests. (A) Fracture surface of nitride 3015, (B) region A$'$ in (A), (C) region A$''$ in (A), (D) magnified image of B$'$ in (B); (E) fracture surface of unnitrided 3015, (F) region E$'$ in (E), (G) E$''$ in (E), (H) magnified image of (G). 42
5.18 SEM images of the fracture surfaces after SSRT from the unnitrided (A–C) and nitrided (D–F) X45CrSi9-3 steel in 0.1 M H_2SO_4 + 3g/L NH_4SCN electrolyte for 2 h at RT using a current density of 0.5mA/cm^2 prior to the tensile test. (A, D) Overview of the fracture surface, (B) magnified images of A$'$ in (A), (C) magnified images of A$''$ in (A),(E) magnified images of D$'$ in (D), (F) magnified images of D$''$ in (D). . . 43

List of Tables

2.1 The nominal chemical composition of the 3015 (wt%) [7]. 4
2.2 The nominal composition of the X45CrSi9-3 investigated (wt%) . . . 4

5.1 Mechanical properties of unnitrided X45CrSi9-3 specimen with and without hydrogen charging. 36
5.2 Mechanical properties of X45CrSi9-3 re-nitrided in Bodycote without hydrogen charging. 37
5.3 Mechanical properties of unnitrided 3015 alloy. 38
5.4 Mechanical properties of nitrided and unnitrided 3015 alloy under different charging conditions. 39

1
Introduction

Hydrogen (H) is a clean energy carrier that is potentially carbon-free and non-toxic, and a successful application will greatly reduce greenhouse gas (GHG) emissions to meet climate goals [2]. The development of hydrogen-based technologies is often constrained by the weakening of properties of specific metallic materials in the presence of hydrogen. A key challenge in this field is hydrogen embrittlement (HE), a process in which the metal's ductility and toughness are significantly reduced upon exposure to hydrogen. This embrittlement occurs as hydrogen atoms interact with the metal's microstructure, weakening it over time [3].
TRATON Group R&D is currently developing next-generation hydrogen-fueled combustion engines to support Sweden's transition towards sustainable energy-based transportation. In these engines, the valves are exposed to high temperatures and a corrosive environment, necessitating the use of 3015 and X45CrSi9-3, high-strength, corrosion-resistant materials [4]. To further enhance performance, a surface treatment will be applied. While chromium-based coatings are commonly used due to their excellent hardness, corrosion resistance, and wear resistance, the (Cr^{+6}) compounds used in conventional chromium electroplating are carcinogenic and subject to the European Union's REACH regulations [5]. There are some options that perform the same function, such as plasma/gas nitriding.
These techniques are widely used to improve the hardness and wear resistance of many metals [6]. Because the entire process is carried out without toxic chemicals, plasma/gas nitriding is a potentially more environmentally friendly alternative to traditional Cr^{+6} coating. However, the behavior of the nitriding layer in a hydrogen-rich environment, particularly its resistance to HE, remains poorly understood and warrants further systematic study.
The purpose of this master's thesis is to examine the effect of a nitriding layer on the mechanical properties of the valve steels under exposure to hydrogen. The aim is to provide new inputs that support replacing conventional chromium electroplating processes involving hazardous Cr(VI) compounds for hydrogen combustion engine valves, contributing to the European Sustainable Development Goals and promoting a hydrogen-based energy economy.
Specifically, the following work was performed: (1) As-received TRATON engine valves with surface treatments produced by gas nitriding and plasma nitriding were examined. The effects of the nitriding process on hardness and hydrogen uptake of the 3015 and X45CrSi9-3 materials were investigated. (2) Small tensile specimens were extracted from the engine valves and subsequently gas nitrided by Bodycote. The re-nitrided specimens were then electrochemically hydrogen charged. The influence of the gas-nitrided layer on hydrogen embrittlement (HE) resistance was

subsequently evaluated.

2

Engine Valve

The materials investigated in this study are engine valves provided by TRATON Group R&D. Engine valves regulate gas exchange in the combustion chamber, allowing intake of air/fuel and expulsion of exhaust gases. The as-received valve consists of a stem and a head. The blue dashed line in Fig. 2.1 represents the boundary between the valve stem and valve head. The valve head is produced from a nickel-chromium austenitic steel, designated 3015, which contains $\tilde{3}$0 wt% Ni, 15 wt% Cr, and small amounts of Nb and Ti as alloying elements. For confidentiality reasons, the actual material supplier and the exact material composition of the 3015 alloy used in this study cannot be disclosed. As a reference, the nominal chemical composition of the NCF 3015-type alloy from the literature [7] is given in Table 2.1. The valve stem consists of two materials: 3015 alloy and EN10090 X45CrSi9-3 (0.45 wt % C, 9 wt % Cr, 3 wt % Si). The two materials were joined by friction welding at a distance of 69 mm from the valve tip (red dashed line in Fig. 2.1). The nominal chemical composition of X45CrSi9-3 is summarized in Table 2.2. These valves were subjected to either plasma nitriding or gas nitriding.

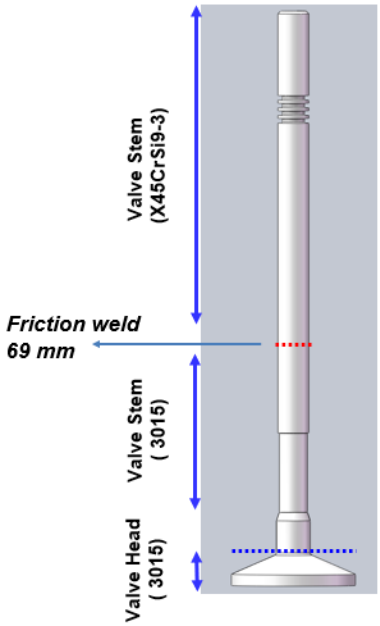

Figure 2.1: Schematic illustration of the engine valve showing the different regions and materials. The red dashed line indicates the friction-welded joint between X45CrSi9-3 and 3015, while the blue dashed line indicates the boundary between the valve stem and valve head.

Table 2.1: The nominal chemical composition of the 3015 (wt%) [7].

Cr	Ni	Ti	Si	Mn	Nb	S	Mb	AI
15	30	2.3 ∼ 2.9	0 ∼ 0.5	0 ∼ 0.5	0.4 ∼ 0.9	0 ∼ 0.1	0.4 ∼ 1	1.6 ∼ 2.2

Table 2.2: The nominal composition of the X45CrSi9-3 investigated (wt%) .

C	Si	Cr	Mn	P	Ni	S
0.45	3	9	0.6	0.04	0.5	0.03

2.1 3015 Alloy

The 3015 type alloy is a precipitation-hardenable iron-nickel-based alloy that offers performance between an iron-based alloy and a more expensive nickel-based alloy, providing high strength, good corrosion resistance, and satisfied high-temperature performance. Due to its excellent strength and corrosion resistance, the 3015 alloy can be used for engine valves and is also considered a replacement material for nickel-based superalloys in applications requiring high strength at high temperatures, such as fasteners and engine valves. [4]. This alloy, after aging, forms strengthening precipitates such as (Ti, Nb)C and Ni_3(Ti, Al), and improves the material's mechanical performance at elevated temperatures up to 700℃ [8]. As Fig. 2.2 (A) shows, the average austenite grain size of 3015 used in this study is approximately 10μm. The different colors in the IPF map indicate different crystallographic orientations, and no visual preferential orientation was observed in the analysis region. The phase map in Fig. 2.2 (B) confirms that the matrix is predominantly FCC austenite, and the black line represents grain boundaries. The EDS element map in Fig. 2.3 shows several particles enriched in Ti, Nb, and C while depleted in Fe and Ni relative to the matrix. This result is consistent with Ti/Nb-rich MC-type carbides, which have been reported in 3015 type alloys.

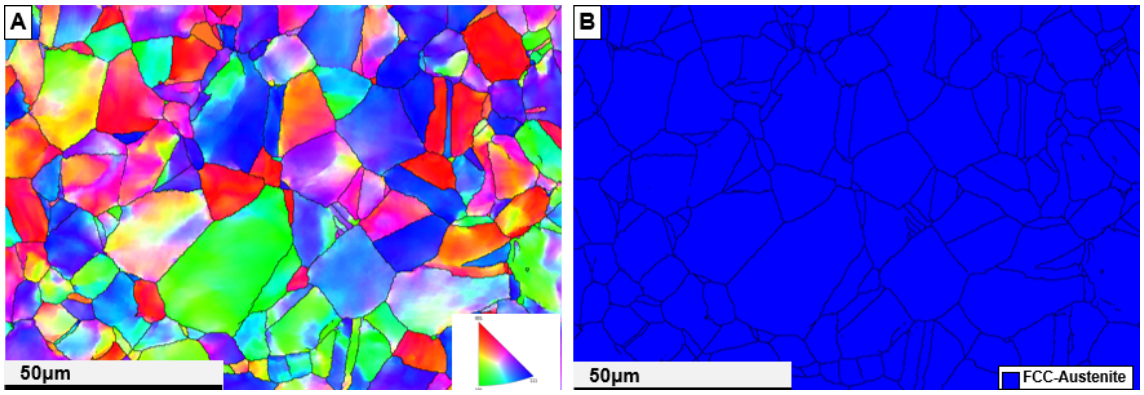

Figure 2.2: IPF map (A) and phase map (B) of 3015 austenitic alloy from the valve stem.

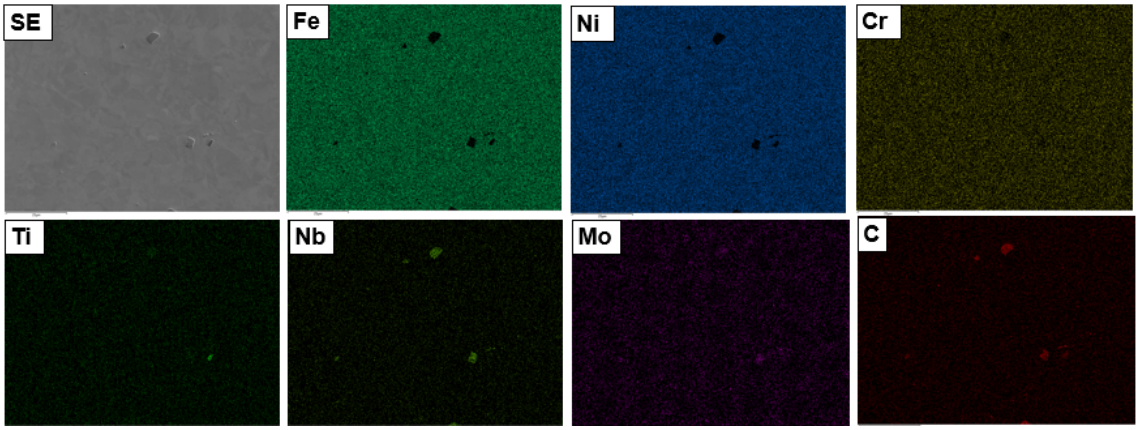

Figure 2.3: EDS element map of 3015 alloy

2.2 X45CrSi9-3 steel

EN10090 X45CrSi9-3 (designation 1.4718) is a martensitic Cr-Si alloyed steel. It is widely used as a valve-stem material in diesel and gasoline engines due to its good oxidation resistance up to 850°C and creep resistance up to 600°C [8]. The steel's chemical composition includes 3% Si and 9% Cr, as seen in Table 2.2. The high silicon content enhances oxidation resistance, while chromium contributes to hardenability and corrosion resistance. After being hardened and tempered, the steel achieves a hardness of HRC 30-40.

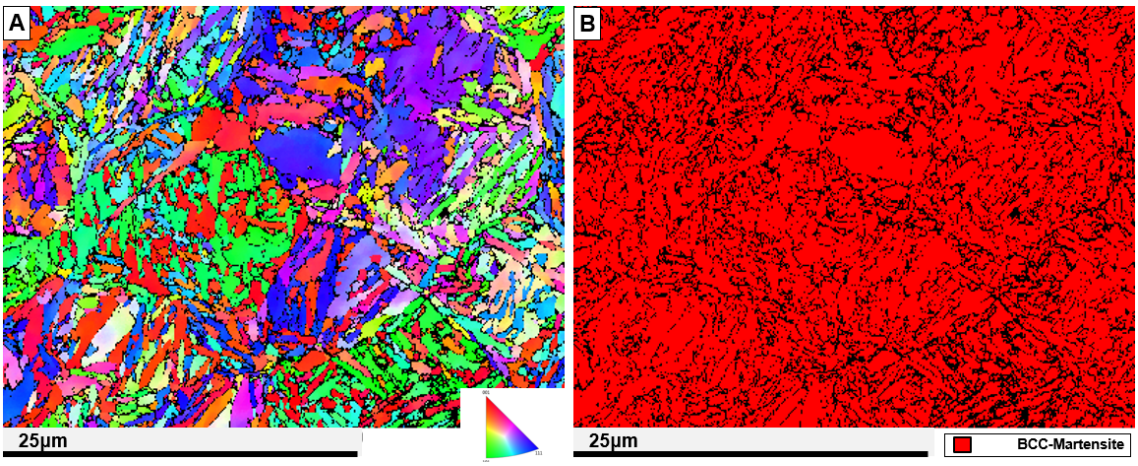

Figure 2.4: IPF map (A) and phase map (B) of X45CrSi9-3 martensitic steel

The EBSD IPF map and phase map of the as-received X45CrSi9-3 material are shown in Fig. 2.4. The IPF map reveals a martensitic microstructure with fine lath-shaped grains of varying crystallographic orientations, consistent with the hardened-and-tempered heat treatment condition. The phase map confirms that BCC martensite is the dominant phase, and only a small fraction of the non-indexing area corresponds to carbides and grain boundaries.

2.3 Nitriding Process

The surface usually refers to the boundary between the machined part and the working environment. It is the first point of load and is directly affected by the environment. Consequently, surface engineering plays a critical role in extending component service life. There are many ways to maintain a durable surface, and nitriding is one of them. Nitriding is a thermochemical treatment that introduces nitrogen into a metallic material. The nitriding process increases surface hardness, enhances wear resistance, and improves the corrosion resistance of the treated material [9].

2.3.1 Gas Nitriding Process

Gas Nitriding is a thermochemical process that maintains the workingpiece at a specific temperature in a controlled environment, allowing nitrogen atoms to diffuse into the sample. It usually includes three process steps: generation of active nitrogen atoms, surface absorption, and diffusion of nitrogen atoms.[10] As a result of the nitriding treatment, the near-surface region of the treated component generally presents high hardness [11], superior tribological performance [12], Superior fatigue performance, and excellent corrosion resistance[13].
High-temperature valve alloys, including martensitic valve steels and iron-nickel-base heat-resistant alloys, have found extensive application in thermomechanically demanding environments, especially in the automotive industry. Gas nitriding can enhance the surface hardness and wear resistance of these alloys, improving their performance and service life in elevated-temperature and chemically aggressive environments.

2.3.1.1 Mechanism of Gas Nitriding

Gas nitriding is a surface-improving process in which nitrogen atoms diffuse into the steel surface by holding the workpiece at an elevated temperature within a controlled nitrogen atmosphere. This process is conventionally carried out using NH_3, $NH_3 + N_2$, or $NH_3 + H_2$ as the reactive process atmosphere. Ammonia(NH_3) thermally decomposes to hydrogen and nitrogen at high temperatures within the furnace according to Eq. 2.1:

$$NH_3 \rightleftharpoons \frac{1}{2}N_2 + \frac{3}{2}H_2 \tag{2.1}$$

Simultaneously, the remaining undecomposed ammonia transfers to the workpiece surface and supplies active nitrogen according to Eq. 2.2.

$$NH_3 \rightleftharpoons [N] + \frac{3}{2}H_2 \tag{2.2}$$

where [N] is nitrogen atom dissolved in steel[13].
Then, the nitrogen atoms diffuse into the metallic surface, forming a nitride layer

that exhibits excellent hardness, wear resistance, corrosion resistance, and fatigue strength compared to the base material. Fig 2.5 presents a schematic illustration of the gas nitriding process.

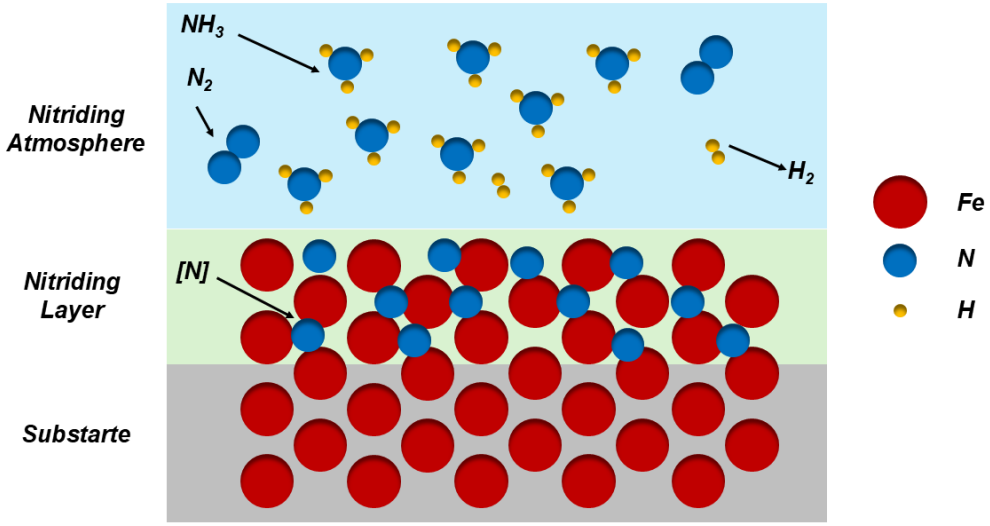

Figure 2.5: Schematic illustration of the gas nitriding process

Gas nitriding forms a nitrogen-rich surface layer on metal samples, and it is called the nitrided layer. The nitrided layer typically consists of a compound layer and a diffusion layer. The outer compound layer is nitrogen-rich and very hard, while the underlying diffusion zone contains a lower nitrogen concentration and provides a combination of strength and toughness due to nitrogen dissolved in the matrix and nitride precipitation[14].

2.3.1.2 Parameters of Gas Nitriding Process

The gas nitriding process parameters mainly include nitriding temperature, nitriding time, atmosphere pressure, and NH3 flow rate. These parameters are mutually interdependent throughout the nitriding cycle and affect the process efficiency.

(1)Nitriding temperature
Nitriding temperature is very important for the process; it significantly affects nitriding layer formation and performance. The typical gas nitriding temperature is around $450 - 580°C$. It has been reported that the nitriding rate accelerates with increasing temperature within a specific temperature range. However, if the temperature is too high, it leads to the formation of an excessive brittle nitrided layer. So, there is an optimal temperature range for different materials. This is because the nitriding temperature affects nitrogen diffusion and nitride formation in the steel[15].

(2)Nitriding time
The nitriding time is the duration the metal samples are exposed to the nitriding

atmosphere. The typical nitriding time is usually between 2 and 60 hours, depending on the material, sample size, and the nitriding depth requirement. In general, longer nitriding time leads to the formation of a thicker nitrided layer. However, an excessively long nitriding duration also results in the coarsening of the grains and an increase in the surface roughness. The relationship between the thickness of the nitrided layer and the processing time is shown in Eq. 2.3

$$X_\alpha \propto \sqrt{Dt} \tag{2.3}$$

where X_α is the layer thickness (m), D is the diffusion coefficient (m^2/s), and t is the diffusion time (s). Assuming that D remains constant during the process, the thickness increases with increasing diffusion time.

(3)Atmospheric pressure
Atmospheric pressure is a vital parameter in gas nitriding. It is typically maintained between 0.1 MPa and 2 MPa. Higher atmospheric pressure results in greater nitriding penetration depth and a faster interface reaction rate, which is highly beneficial for forming a dense, high-hardness nitrided layer [16].

(4)Gas Flow Rate
During gas nitriding, the flow rate of nitrogen or ammonia gas is also an important factor. The flow rate typically ranges from 5 L/min to 50 L/min and critically affects the efficiency of ammonia decomposition during the nitriding process. Some studies show that increasing the flow rate can significantly increase the nitriding rate and the depth of the nitrided layer. However, excessively high nitrogen flow not only increases nitriding costs but also leads to the accumulation of nitrogen atoms in the layer, which creates cracks and pores that reduce workpiece quality [17].

2.3.2 Plasma Nitriding Process

Plasma nitriding, also known as ion nitriding, is a modern low-pressure thermochemical treatment that uses glow-discharge plasma to introduce nitrogen atoms into the surface of metallic components. This process is carried out in a furnace containing a mixture of nitrogen, hydrogen, and an optional carbon-consuming gas, where an electric field is applied. When a voltage is applied between the workpiece (acting as a cathode) and the furnace wall (acting as an anode), a plasma (ionized gas) forms around the metal specimen, and nitrogen ions bombard its surface. These nitrogen ions penetrate deep into the surface and create a hard nitriding layer, which increases the wear, fracture resistance and corrosion resistance of metal component's [18].

2.3.2.1 Mechanism of Plasma Nitriding

The Plasma nitriding process can be divided into three steps:
(1)Generation of active nitrogen species. Under applied voltage and low pressure, the mixture of nitrogen and hydrogen gas can be ionized and form glow-discharged

N^+, N, H^+, and electrons.
(2)Surface interaction. Previously formed conductive gas (plasma) that contained nitrogen ions is accelerated towards the cathode due to the applied electric field and bombards the workpiece surface with high energy, where they sputter-clean the surface, dissociates, and is absorbed as atomic nitrogen. This creates a high nitrogen activity at the interface[19].
(3)Diffusion and layer formation. The absorbed nitrogen atoms are attracted to the workpiece, adsorb on its surface, and subsequently diffuse into the subsurface region. This will lead to the formation of an outer compound layer (white layer) and an inner diffusion layer. The compound layer is located at the surface and is composed of iron nitrides including nitrogen-richer ε-nitride $Fe_{2-3}N$ and the iron-richer γ'-nitride Fe_4N [20].
Compared with gas nitriding, the compound layer is more compact, resulting in less porosity and better layer properties. For the process time, plasma nitriding also requires less holding time, usually around 12-50 hours, half the time required by gas nitriding [19].

3

Hydrogen Embrittlement

3.1 Hydrogen Uptake

In the context of steel exposed to a hydrogen-containing environment, hydrogen can be absorbed into the material. To study hydrogen embrittlement, hydrogen is introduced into the material using one of two methods: electrochemical or gaseous hydrogen charging. Although the gaseous hydrogen charging method can simulate some service environments, it requires a more complex, more expensive system to implement. By contrast, cathodic hydrogen charging is cheaper, safer, and easier to operate, so it is widely used in fundamental studies of hydrogen. In this method, the specimen serves as the cathode and is immersed in the electrolyte. During the process, hydrogen is generated on its surface through the cathodic hydrogen evolution reaction. This reaction follows the Volmer-Tafel-Heyrovsky mechanism, which involves sequential hydrogen adsorption and the formation or desorption of molecular hydrogen. The individual steps are described below. [21].
a) Volmer reaction: During the Volmer step, a proton receives an electron at the cathode and becomes an adsorbed hydrogen (H_{ad}) atom on the metal (M) surface. This reaction represents the electrochemical generation of surface hydrogen. The electrochemical hydrogen adsorption process in an acidic solution can be described as Eq. 3.1.

$$\mathrm{M} + \mathrm{H}^+ + e^- \rightarrow \mathrm{M}{-}\mathrm{H}_{\mathrm{ad}} \tag{3.1}$$

In a neutral or alkaline medium, the Volmer reaction is described by Eq. 3.2.

$$\mathrm{M} + \mathrm{H_2O} + e^- \rightarrow \mathrm{M}{-}\mathrm{H}_{\mathrm{ad}} + \mathrm{OH}^- \tag{3.2}$$

b) Tafel reaction: In the Tafel reaction, two adsorbed hydrogen (H_{ad}) atoms recombine and form molecular hydrogen on the metal surface. This step does not involve electron transfer and removes the adsorbed hydrogen from the surface. This step can be described as Eq. 3.3.

$$2\mathrm{M}{-}\mathrm{H}_{\mathrm{ad}} \rightarrow 2\mathrm{M} + \mathrm{H_2(g)} \uparrow \tag{3.3}$$

c) Heyrovsky reaction: In the Heyrovsky step, an adsorbed hydrogen (H_{ad}) atom reacts with another proton and an electron from the electrolyte solution and forms hydrogen gas. This reaction also removes the adsorbed hydrogen from the surface, similar to the Tafel step. In an acidic solution, it can be described as Eq. 3.4.

$$\mathrm{M}{-}\mathrm{H}_{\mathrm{ad}} + \mathrm{H}^+ + e^- \rightarrow \mathrm{M} + \mathrm{H_2(g)} \uparrow \tag{3.4}$$

In a neutral or alkaline medium, the Heyrovsky reaction is described as Eq. 3.5.

$$\mathrm{M{-}H_{ad}} + \mathrm{H_2O} + e^- \rightarrow \mathrm{M} + \mathrm{OH^-} + \mathrm{H_2(g)} \uparrow \tag{3.5}$$

d) Hydrogen absorption: The adsorbed hydrogen (H_{ad}) can subsequently diffuse into the metal and be converted into absorbed hydrogen (H_{ab}), which can be described by Eq. 3.6.

$$\mathrm{M{-}H_{ad}} \rightarrow \mathrm{M{-}H_{ab}} \tag{3.6}$$

3.2 Hydrogen Solubility and Diffusion

Once hydrogen is absorbed, it diffuses into the material's structure and seeks a thermodynamically favourable site with the lowest energy. In a perfect crystal, hydrogen atoms are preferentially located at BCC tetrahedral or FCC octahedral interstitial sites. However, in practice, high hydrogen content can be observed in different trap sites, such as grain boundaries, vacancies, and dislocations, as shown in Fig 3.1.

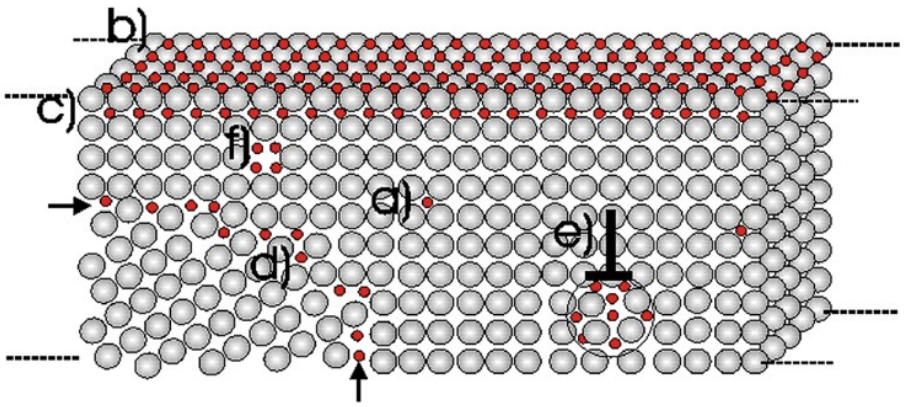

Figure 3.1: Schematic of hydrogen traps in steel:(a) interstitial sites; (b) surface traps; (c) subsurface traps; (d) grain boundary traps; (e) dislocation traps; (f) vacancy traps [23]

In general, diffusion can be expressed by Fick's first and second laws. Fick's first law describes steady-state diffusion, as shown in Eq 3.7.

$$J = -D\frac{\partial C}{\partial x} \tag{3.7}$$

Where J represents the diffusion flux, D represents the diffusion coefficient, x is the depth from the surface, and $\frac{\partial C}{\partial x}$ is the concentration gradient. J and $\frac{\partial C}{\partial x}$ stay constant with time in steady-state diffusion. The negative sign here (Eq 3.7) means that J always flows from the higher concentration region to the lower concentration region.

Fick's second law describes the non-steady state diffusion, and here the concentration changes with time and diffusion distance, and it can be expressed in Eq 3.8. In this study, Fick's second law is the more relevant equation because hydrogen enters the material from the surface, and hydrogen concentration changes with time and depth below the charged surface during hydrogen charging.

$$\frac{\partial C}{\partial t} = D\frac{\partial^2 C}{\partial x^2} \tag{3.8}$$

where $\frac{\partial C}{\partial t}$ represents the changes in concentration over time, and $\frac{\partial^2 C}{\partial x^2}$ is second derivative of concentration for distance. This law governs how hydrogen redistributes within the steel after uptake at the surface.
The actual hydrogen diffusion speed depends on several factors, such as temperature, microstructure, pressure, and defects. The hydrogen diffusion coefficient D is an important parameter for evaluating hydrogen diffusivity and can be expressed by the Arrhenius equation Eq 3.9

$$D = D_0 \exp\left(-\frac{Q}{RT}\right) \tag{3.9}$$

Where D_0 is the pre-exponential factor or Arrhenius factor. Q is the activation energy, which depends on the crystal structure and diffusion element, and T is the temperature. D is a temperature-dependent parameter.

It is important to note that hydrogen solubility in pure iron is also temperature-dependent, as phase transformations in the metal alter the crystal structure. Figure 3.2 shows the hydrogen solubility in pure iron as a function of temperature. It is very low at lower temperatures. Various iron phases also have different solubilities. The austenite (γ-Fe) phase has the highest solubility in the solid state, while Ferrite (α-Fe) exhibits the lowest one. However, in all phases, hydrogen solubility increases rapidly with increasing temperature. As discussed before, different types of trap sites can absorb large amounts of hydrogen. The trap sites shown in Fig. 3.1 can be classified based on their activation energy (E_b). When $E_b < 60$ kJ mol$^-$, the trap is generally considered a reversible hydrogen trap, from which hydrogen can be released during desorption. Reversible traps include interstitial sites, dislocations, lath boundaries, grain boundaries, and coherent precipitates. When $E_b > 60$ kJ mol$^-$, the trap is generally classified as an irreversible hydrogen trap. Carbides, inclusions, and incoherent precipitates belong to irreversible hydrogen traps.

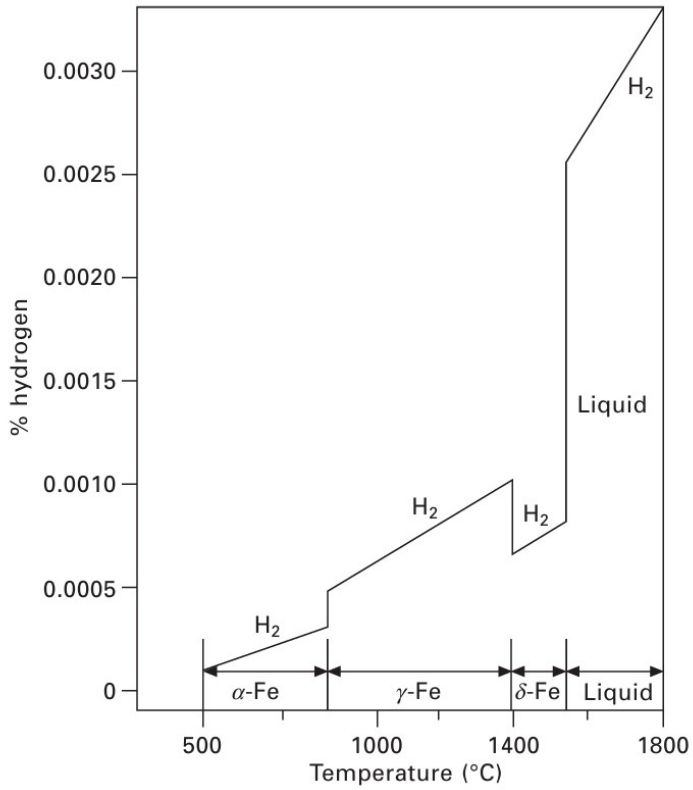

Figure 3.2: Hydrogen solubility in pure iron as a function of temperature. (Hydrogen (H) contents expressed in wt%) [24]

3.3 Mechanism of Hydrogen Embrittlement

In the late 19th century, the concept of hydrogen embrittlement was first observed by Johnson [22]. Since then, numerous studies have been conducted to understand the mechanisms underlying HE. In this section, several HE mechanisms that have been proposed to explain HE phenomena so far are listed.

3.3.1 Hydrogen Pressure Theory

The hydrogen pressure theory was originally introduced by Zapffe et al. [25] in 1941. According to this theory, hydrogen atoms tend to concentrate on lattice defects within metallic materials, such as microvoids and inclusions. As these hydrogen atoms combine to form H_2, they create gas pressure within the material. With increasing exposure time, more hydrogen atoms migrate to defect sites, thereby increasing hydrogen gas pressure and leading to hydrogen-induced cracking when internal hydrogen gas pressure surpasses the material's strength limit.

3.3.2 Hydrogen-Enhanced Localized Plasticity Mechanism (HELP)

In 1972, Beachem [26] proposed the Hydrogen-Enhanced Localized Plasticity Mechanism (Figure 3.3) to explain hydrogen-assisted cracking. In this mechanism, hydrogen atoms accumulate near the crack tip and facilitate dislocation motion, thereby promoting localized plastic deformation in the metal lattice. The presence of hydrogen near a dislocation reduces the local resistance to dislocation motion, thereby enabling dislocation motion at lower stress levels. Several studies support this mechanism. Birnbaum, Robertson, and Sofronis [27, 28, 29] performed in situ TEM experiments and demonstrated that the presence of hydrogen can increase dislocation mobility under constant stress conditions. In stressed specimens, dislocation mobility was enhanced upon introducing H_2 into the environment and was reduced after H_2 was removed. This behavior has been observed for edge, screw, and mixed dislocations, as well as for isolated dislocations and dislocation tangles.

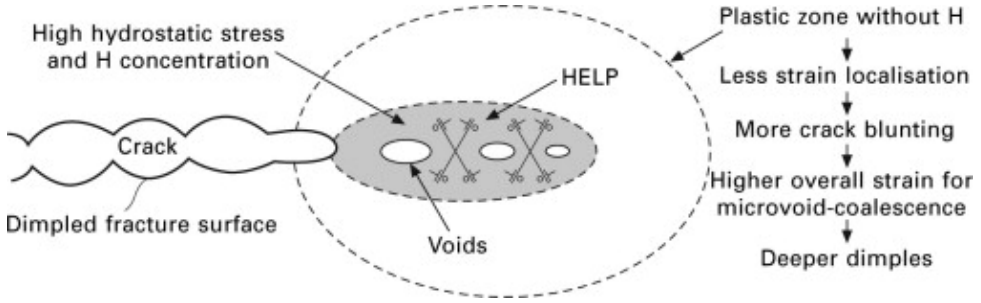

Figure 3.3: Schematic of HELP mechanism [23]

3.3.3 Hydrogen-Enhanced Decohesion Mechanism (HEDE)

The Hydrogen-Enhanced Decohesion Mechanism is a simple mechanism and was first introduced by Pfeil in 1926 [30], who proposed that hydrogen atoms decrease the cohesive strength between atoms, especially at grain boundaries and phase interfaces. In 1959, Troiano proposed that the electron in the 1s orbit in a hydrogen atom is likely to enter an unfilled 3d orbit in a metal. This increases the repulsive force between atoms and thus reduces atomic bonding strength. For decohesion to occur, sufficiently high hydrogen concentration is required. However, due to the lower solubility of hydrogen in metals (except for a few elements like Pd), hydrogen is usually homogenously distributed in the microstructure. It has been proposed in some studies that high hydrostatic stresses, including strain-gradient hardening, can lead to high hydrogen concentrations [32]. Suggested decohesion locations [23, 33] are: (1) sites with adsorbed hydrogen atoms at crack tips, (2) dislocation shielding regions at crack tips, (3) grain boundaries and interphase boundaries at crack tips, (4) sites of maximum hydrostatic stresses, and (5) particle/matrix interfaces (Figure 3.4).

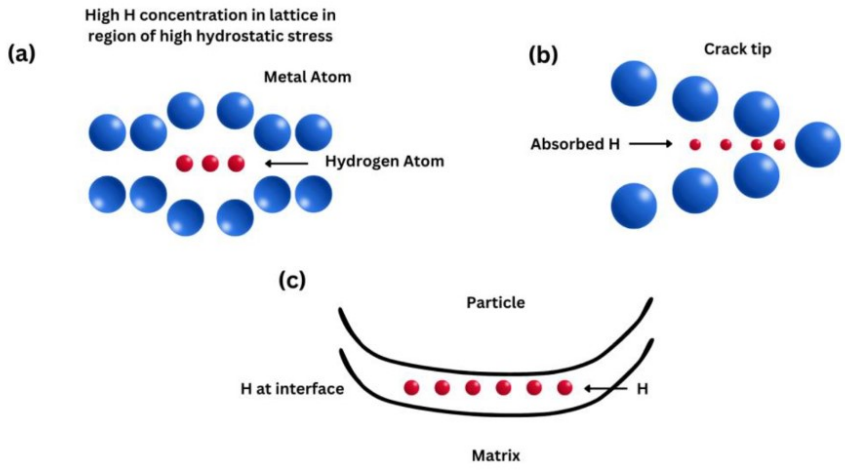

Figure 3.4: Schematic diagrams illustrating the HEDE mechanism, showing tensile separation of atoms caused by hydrogen-induced weakening of interatomic bonds by (a) hydrogen in the lattice, (b) hydrogen adsorbed at crack tips, and (c) hydrogen at particle–matrix interfaces. [31]

3.3.4 Adsorption-Induced Dislocation Emission (AIDE)

Lynch first proposed the AIDE mechanism in 1976 [34]. This mechanism combines aspects of both HEDE and HELP mechanisms. However, it is more complex than either mechanism alone. In this mechanism, hydrogen first adsorbs at the crack tip, where it weakens interatomic bonding and cohesive strength via the HEDE mechanism. Hydrogen adsorption then promotes the emission of dislocations. The resulting enhanced localized plasticity facilitates crack propagation by slip bands and formation of microvoids through the HELP mechanism (Figure 3.5). In AIDE, hydrogen adsorption promotes decohesion and dislocation emission at crack tips, leading to crack nucleation and growth. The combined effects of slip coalescence and micro voids result in crack growth and fracture [35].

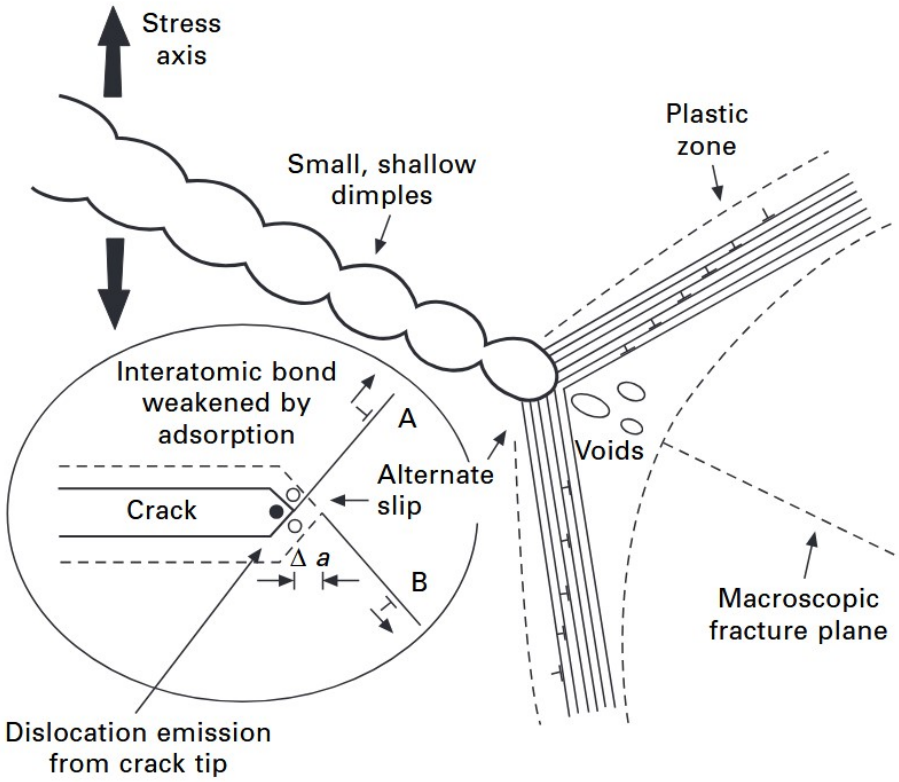

Figure 3.5: Schematic diagram illustrating the adsorption-induced dislocation emission (AIDE) mechanism [36]

4

Methods

4.1 Sample Preparation

4.1.1 Metallographic Specimen

The metallographic specimens were cut directly from the engine valve with a thickness of 2.3 mm and then mounted in conductive resin. Grinding was carried out sequentially using 1000#, 2000#, and 4000# SiC papers, followed by polishing using 3μm and 1μm diamond suspensions with OPS (oxide polishing suspension) as the final step. To reveal the microstructure, the samples were etched with V2A reagent (119 mL HCl, 12mL HNO_3, 119 mL H_2O) for 20s at room temperature.

4.1.2 Tensile Test Specimen

Limited by the geometry of the engine valve, small tensile test specimens, as shown in Fig 4.1, were used in this study. The dog-bone-shaped specimens having a thickness of 1mm were extracted from the valve stem by means of electrical discharge machining (EDM). To remove the hard, brittle white layer formed during the EDM process, each tensile specimen was manually ground with 2000# SiC paper for 1 min on each surface, followed by ultrasonic cleaning in ethanol for 20 min.

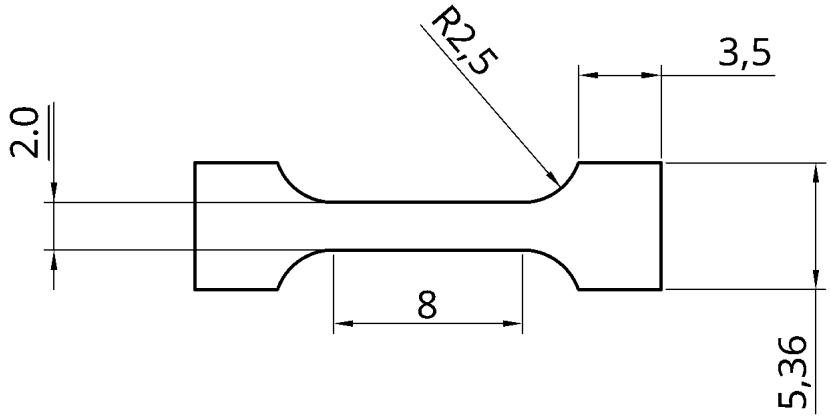

Figure 4.1: Geometry of tensile test specimen

4.1.3 Nitrided Specimen

Nitriding is a thermochemical treatment that introduces nitrogen into a metallic material. In this work, the as-received engine valve has been subjected to two different nitriding treatments: gas nitriding and plasma nitriding. Plasma nitrided engine valves have an approximately 8.8 μm–9.3 μm thick nitriding layer, while gas nitrided engine valves have a 12.6 μm – 16.2 μm thick nitriding layer. Because the nitriding layer was not preserved during sample preparation, the extracted samples underwent re-nitriding at Bodycote Värmebehandling AB. This is a low-temperature gas nitriding process performed at 510°C for 60 hours in a 1:1 mixture of gaseous NH_3 and N_2, with a gas flow rate of approximately $5m^3$/h. The specimens were heated from 80 to 510 °C at a heating rate of about 4 °C/min. After the nitriding treatment, the specimens were gas-cooled in a N_2 atmosphere from 510 °C to 100 °C at a cooling rate of about 2.5 °C/min. This process forms a nitrided layer on the specimen surface. The layer thickness is around 30 μm and hardness can reach up to 1400 HV.

4.2 Cathodic Hydrogen Charging

In this study, hydrogen was introduced into the materials using an electrochemical cathodic charging method (Fig 4.2). The typical parameters that significantly affect hydrogen uptake include electrolyte, charging current, temperature, and charging duration. Common electrolytes used for hydrogen charging include H_2SO_4, NaCl, and NaOH aqueous solutions. The high concentration of H^+ ions provided by H_2SO_4 results in substantially higher hydrogen generation compared with NaCl and NaOH solutions. H_2SO_4 is also widely used to simulate hydrogen uptake in highly aggressive service environments. Therefore, in this study, an H_2SO_4 electrolyte solution was selected as the source of hydrogen, with 3 g/L NH_4SCN added as a hydrogen recombination poison to prevent the recombination of adsorbed hydrogen atoms at the metal surface, thereby promoting hydrogen absorption into the material. The electrochemical cathodic charging was conducted at room temperature (RT), 52°C and 80°C, with a current density ranging from 0.5 to 30 mA/cm^2 and a charging duration of 2-24 hours.

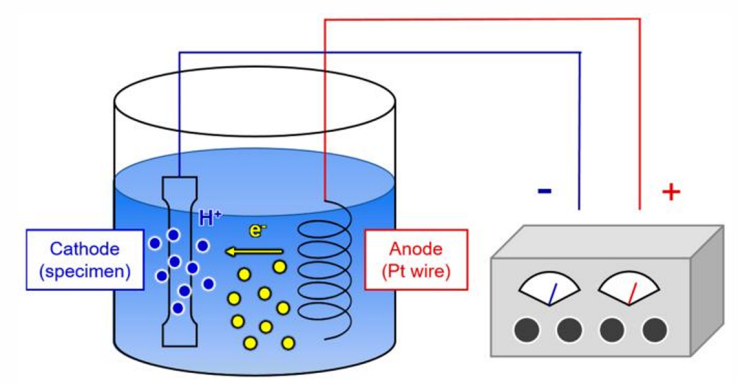

Figure 4.2: Schematic illustration of an electrochemical hydrogen charging setup

4.3 Characterization Techniques

4.3.1 Optical Microscopy (OM)

An optical microscope is also known as a light microscope. It is the oldest type of microscope and uses visible light together with a lens system to produce magnified images of small specimens. The maximum resolution of an optical microscope is typically around 200 nanometers due to the diffraction limit imposed by the wavelength of visible light. Due to its high resolution, ease of operation, and low cost, OM is well-suited and widely used in biotechnology, mineralogy, and the study of metallic materials. There are two basic types of optical microscopes: simple microscopes and compound microscopes. The vast majority of modern research microscopes are compound microscopes, which use a system of lenses to achieve a much higher magnification of an object, as shown in Fig 4.3. In this thesis, OM images were obtained using a Zeiss Axioscope 7 optical microscope.

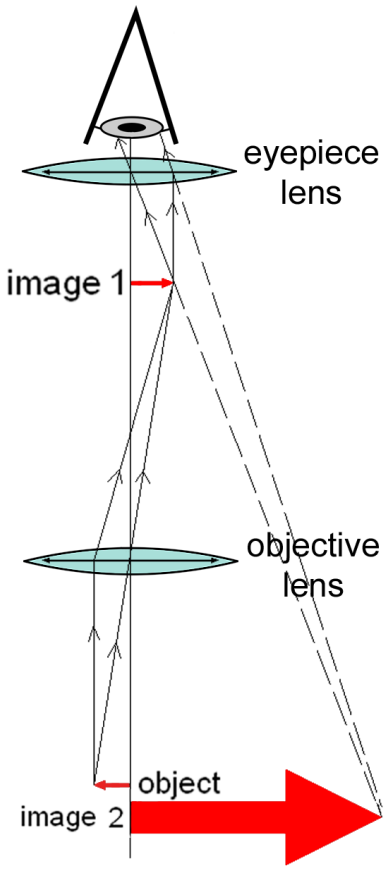

Figure 4.3: Diagram of a compound microscope [37]

4.3.2 Scanning Electron Microscopy (SEM)

SEM is a type of electron microscopy that produces magnified images of a sample by scanning it with a focused beam of electrons. In a SEM, electrons emitted from the electron gun are accelerated by an electric field and pass through a series of

condenser lenses, electromagnetic coils, and an aperture before being focused into a finely convergent beam that scans the surface of the specimen. When electrons hit the sample surface, they generate various types of signals that provide information about surface topography and composition, including auger electrons, secondary electrons, back-scattered electrons, characteristic X-rays, and continuum X-rays (Fig 4.4). In this work, the microstructure and surface morphologies of the materials were examined using Zeiss Gemini 450 FE-SEM and LEO Gemini 1550 FE-SEM. The accelerating voltage was set at 5-20 keV, and the working distance was around 8-15 mm.

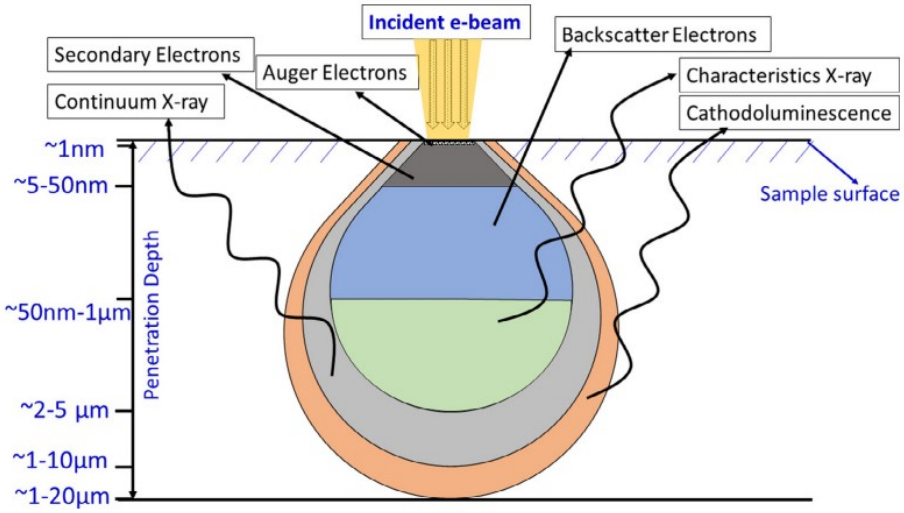

Figure 4.4: Schematic diagram showing the SEM interaction volume with dimensions. [38]

4.3.3 Electron Backscatter Diffraction (EBSD)

Electron back-scatter diffraction (EBSD) is a powerful SEM technique used to study the crystallographic structure of materials. In a SEM equipped with an EBSD detector, when the sample surface is irradiated by the incident beam of electrons, a fraction of high-energy backscattered electrons undergo Bragg diffraction by the crystal lattice, forming Kikuchi bands, which are then projected onto a phosphor screen to produce an EBSD pattern. The diffraction pattern is determined by the distance between lattice planes and the crystal structure of the material under study. The spatial resolution of EBSD is affected by many factors, including the material's nature and sample preparation. EBSD indexes the acquired Kikuchi patterns by matching them with simulated patterns generated from known crystal structure databases. This process provides detailed crystallographic information, including grain orientation, phase distribution, and grain boundary character at the microscale [39].

Fig 4.5 shows the EBSD setup schematically. During the experiment, the sample needs to be tilted 70° to increase the signal intensity reaching the EBSD detector. In this work, EBSD phase maps and the Inverse pole figure (IPF) map were performed using a Zeiss Gemini 450 FE-SEM and a LEO Gemini 1550 FE-SEM, both coupled

with a Symmetry detector. The accelerating voltage was set to 20 keV, and the working distance was 15 mm. The scan step size of EBSD map acquisition was 0.1-5μm.

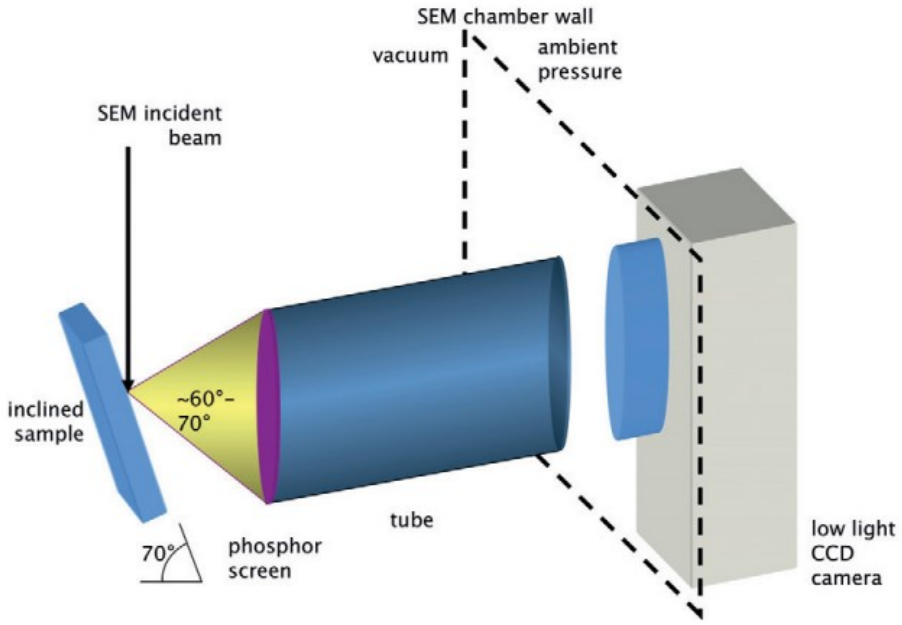

Figure 4.5: Schematic experimental set-up for EBSD collection. [39]

4.3.4 Hydrogen Measurement

Thermal desorption spectroscopy (TDS) is an analytical technique used to quantify and characterize trapped gas or volatiles in the sample. It is also very useful for hydrogen. In TDS, pre-charged samples are gradually heated in a controlled environment, and the released hydrogen flux is monitored with mass spectrometry (MS) or a thermal conductivity detector (TCD). The information that can be extracted includes hydrogen concentration, diffusivity, and trapping characteristics (binding energies and trap densities). In contrast, inert gas fusion (IGF) is used to determine the total hydrogen content by melting the specimen in an inert atmosphere, where the released gas is detected by TCD. In this study, the total hydrogen content was measured using a Bruker G8 GALILEO ONH analyzer based on inert-gas technology. Diffusible hydrogen was measured by a Bruker G8 GALILEO ONH analyzer equipped with an external IR07 infrared furnace. The samples were heated at a rate of 0.97℃/S to 900 °C and held at this temperature for 900 s to extract the diffusible hydrogen.

4.4 Mechanical Testing

4.4.1 Hardness Test

Hardness testing measures a material's resistance to localized permanent deformation by applying a specific force to its surface. Material hardness is generally correlated with strength, wear resistance, and toughness. Materials with high hardness usually show higher strength and better wear resistance, but may also have reduced ductility and increased brittleness. In contrast, materials with low hardness tend to be more ductile and can undergo larger plastic deformation before fracturing. Common methods for hardness testing include the Rockwell test, which measures indentation depth; the Brinell test, which determines hardness from indentation area; and Vickers/Knoop tests, which employ diamond pyramid indenters to evaluate microhardness. In this study, the Vickers hardness method was selected because the nitride layer was only (10-20 μm) thick, requiring a low-load indentation technique capable of accurately characterizing thin surface layers. It uses a square-based diamond pyramidal indenter with an angle of 136° between opposite faces. According to ASTM E384-22 standard, the Vickers hardness is calculated using Eq. 4.1

$$HV = 1854.4 \times \frac{P}{d^2} \tag{4.1}$$

Here P is the applied force (gf) and d is the mean diagonal length of Vickers indentation (μm). Microhardness measurements were performed on the polished cross-sections using a DualScan 70 G5 micro-Vickers hardness tester under a load of 10 gf. To avoid overlap of deformation zones, the distance between adjacent indentations was larger than $3d$. At each depth, the reported hardness value represents the average of three measurements.

4.4.2 Slow Strain Rate Tensile Test

The slow strain rate tensile test was conducted according to ASTM E8M-22 [40]at ambient temperature using universal testing machines (Instron 5500R, USA, and Kammrath & Weiss, Germany) under constant strain rate of $1 \times 10^{-4} s^{-1}$. For the samples subjected to electrochemical hydrogen charging, tensile testing was performed immediately after the completion of the charging to minimize hydrogen loss before testing. Hydrogen embrittlement susceptibility was evaluated using the hydrogen embrittlement index (HEI) δ_L, as defined in Eq. 4.2.

$$\delta_L = \frac{\delta_0 - \delta_H}{\delta_0} \times 100\% \tag{4.2}$$

Here δ_0 and δ_H are the total elongation of the uncharged and hydrogen-charged samples, respectively. In general, a higher δ_L indicates higher plasticity loss and higher susceptibility to hydrogen embrittlement.

5

Results and Discussion

5.1 Microstructure

5.1.1 As-Received Engine Valve

The engine valves supplied by TRATON are manufactured by friction-welding two different materials: X45CrSi9-3 and 3015. The valve surface has an 8-20 μm-thick nitriding layer, depending on the nitriding process. This section presents the microstructure results from the valve stem for gas-nitrided and plasma-nitrided engine valves, as shown in Fig. 5.2 and Fig. 5.3. The representative sampling regions are illustrated in Fig. 5.1. To examine the spatial variation of the nitrided layer, additional observations at specific locations on the valve head, namely the valve face and valve bottom, were performed, as presented later in Fig. 5.6.

As shown in Fig. 5.2, for a gas-nitrided engine valve, the nitriding layer thickness is around 12.6μm for the 3015 alloy, while it is around 16.2μm for X45CrSi9-3. As shown in Fig. 5.3, for a plasma nitrided engine valve, the nitriding layer is thinner than that formed by the gas nitriding process. The thicknesses are approximately 8.8 mum and 9.3 mum for the 3015 and X45CrSi9-3, respectively.

In both nitriding processes, the 3015 alloy has a thinner nitriding layer than X45CrSi9-3. This difference in case depth can be attributed to several factors. First, the microstructures of the two materials differ. K. Hussain et al.[41] find that the case depth of the nitriding layer decreases with the increase of austenitic content, because nitrogen diffuses much faster in the body-centered cubic (BCC) martensitic phase than in the face-centered cubic (FCC) austenitic phase. Using the data in the reference book [42], it has been found that there is a difference in the diffusion behavior of austenitic and martensitic structures, as shown in equation 5.1

$$D_{\alpha}^{\mathrm{N}} \approx 10^{4} \times D_{\gamma}^{\mathrm{N}} \tag{5.1}$$

where D_{α}^{N} and D_{γ}^{N} are the diffusion coefficients of nitrogen atoms in FCC and BCC structures, respectively.

The second is the alloying element. Widi et al. [43] reported that chromium has a higher affinity for nitrogen atoms during nitriding than other alloying elements. The 3015 part of the valve stem contains 15% Cr, while the X45CrSi9-3 part contains only 9% Cr. This difference, together with the higher solubility of N in fcc austenite, may contribute to the accumulation of nitrogen near the surface in the 3015 alloy, which may lead to a thinner case depth.

The third and most important reason is that this nitriding process is optimized

for X45CrSi9-3 because the stem requires a nitrided layer and most of the stem is made of X45CrSi9-3. Also, the X45CrSi9-3 part of the valve stem is polished after nitriding to achieve a smooth surface, while the 3015 part remains unpolished.

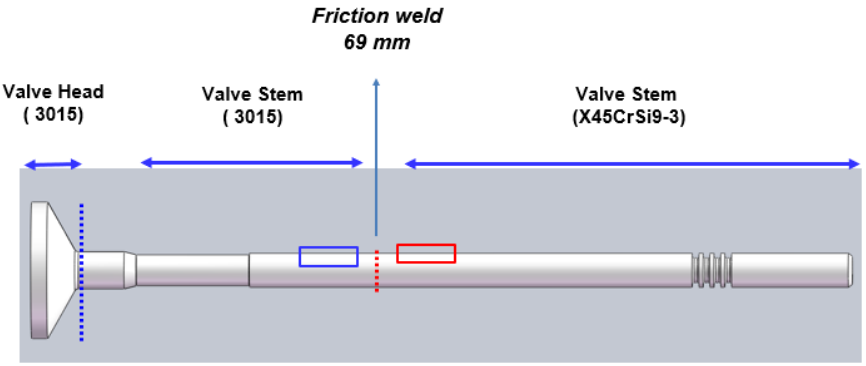

Figure 5.1: Schematic illustration of the engine valve materials and regions. Blue and red boxes indicate sampling locations for microstructural analysis of 3015 and X45CrSi9-3, respectively.

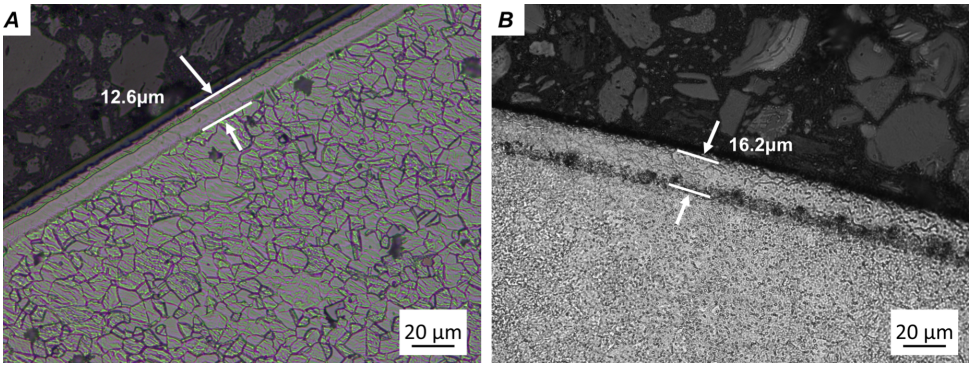

Figure 5.2: Microstructure of gas nitrided engine valve:(A) 3015 alloy, (B) X45CrSi9-3

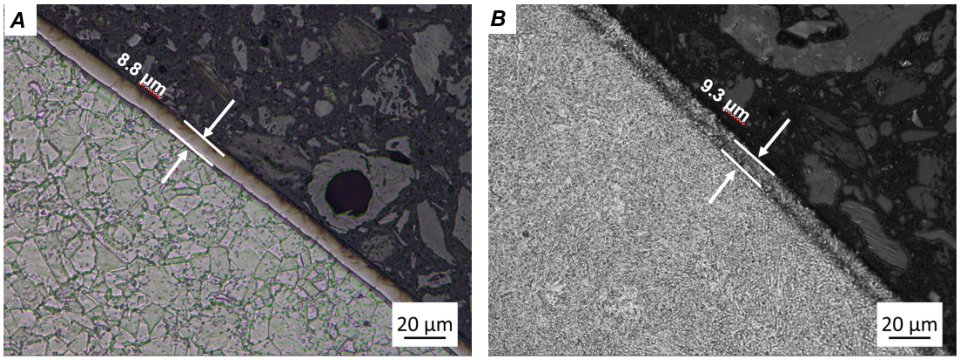

Figure 5.3: Microstructure of plasma nitrided engine valve:(A) 3015 alloy, (B) X45CrSi9-3

The thickness of the nitrided layers differed between gas nitriding and plasma nitriding. The first reason is the difference in process parameters. As mentioned in the previous section, several key parameters influence the nitriding layer's features, including temperature, atmosphere, nitriding time, gas pressure, and flow rate. For confidentiality reasons, the exact process parameters used by the supplier are unknown; however, the differences in nitriding layer thickness are consistent with the known effects of these parameters. In addition to total nitrided layer thickness, the outer compound layer thickness may also differ in plasma and gas nitriding processes. The compound layer is the surface nitride-rich layer formed during nitriding, while the underlying diffusion zone contains dissolved nitrogen in the matrix. In this study, however, we could not reliably separate the distinct compound layer from the diffusion zone using an optical microscope or SEM. The EDS analysis in Fig. 5.5 shows elemental changes near the surface, but we use this result only for qualitative analysis because EDS is insensitive to light elements like nitrogen. Therefore, this study does not quantitatively analyze compound layer thickness. Nevertheless, many studies have reported differences in compound layer formation between gas nitriding and plasma nitriding. Gas nitriding typically forms a thicker compound layer than plasma nitriding. This aligns with the intrinsically lower nitriding potential of the plasma process, which usually limits surface nitrogen activity and restricts compound-layer growth [44]. Furthermore, plasma nitriding involves several parallel processes, including activation, implantation, sputtering, and adsorption. In addition, H_2 in the plasma nitriding atmosphere continuously reduces and sputters the specimen surface, thereby suppressing excessive formation of a brittle compound layer [45]. As a result, plasma nitriding forms a thin and more controllable compound layer. Peng et al. [46] also reported that the compound layer can be precisely controlled by adjusting the nitrogen and hydrogen ratio.

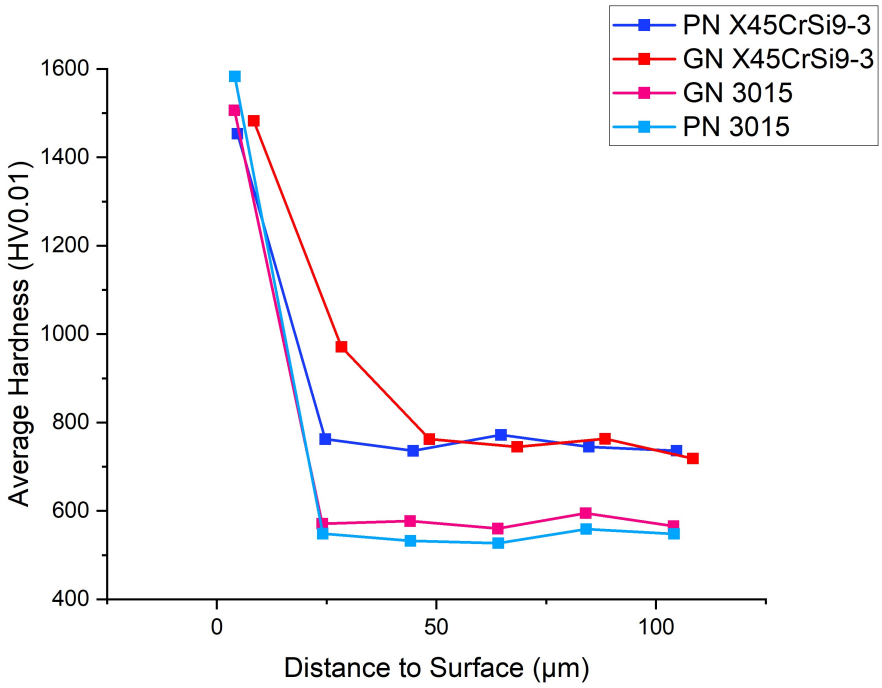

Figure 5.4: Vickers microhardness profiles as a function of distance from the surface for Plasma Nitrided (PN) and Gas Nitrided (GN) treated X45CrSi9-3 and 3015 steels.

Figure 5.4 shows the Vickers microhardness profiles as a function of distance from the surface for plasma and gas nitrided 3015 alloy and X45CrSi9-3 steel. The measurements were performed using a 0.01kg load, with a spacing of 20 μm between adjacent indentations. The hardness profile shows that the highest hardness was measured on the top nitrided surface for all conditions, reaching approximately 1400- 1600 HV0.01. Hardness then decreases rapidly with increasing distance from the surface and reaches the constant base-material hardness value. The substrate hardness value for X45CrSi9-3 is around 720-780 HV0.01 for X45CrSi9-3, and 520-590 HV0.01 for 3015, respectively. Importantly, the substrate material showed similar hardness values for the gas and plasma nitrided samples, indicating that the difference between the two nitriding processes is mainly related to the near-surface region. The hardness profile gives a clear overview of the variation in hardness with depth. It also provides an approximate indication of the effective case depth rather than a direct measurement of the exact thickness of the nitriding layer.
Figure 5.5 presents the EDS line scan profiles of Fe, Ni and N for plasma and gas nitrided 3015 alloy and X45CrSi9-3 steel. The profiles show the relative signal intensities of these elements as a function of depth from the surface, providing qualitative information on the elemental distribution across the nitrided layer. In particular, the N signal is strongest at the top of the nitriding layer and decreases with depth, while the Cr and Fe signals increase towards the substrate. This trend suggests that N atoms diffused into the surface region during nitriding, resulting in an increase in the content of N in the upper layer and a corresponding decrease in the Cr and

Fe contents. The measured nitrogen-enriched depth is roughly consistent with the nitrided layer thickness observed by OM (Fig 5.2, Fig 5.3), which was 12.6 μm for Gas nitrided 3015, 16.2 μm for gas nitrided X45CrSi9-3, 8.8 μm for plasma nitrided 3015, and 9.3 μm for plasma nitrided X45CrSi9-3, respectively. As discussed previously, the higher amount of Cr present in the 3015 alloy, together with its high affinity with N, results in a thinner nitriding layer than that in X45CrSi9-3 steel.

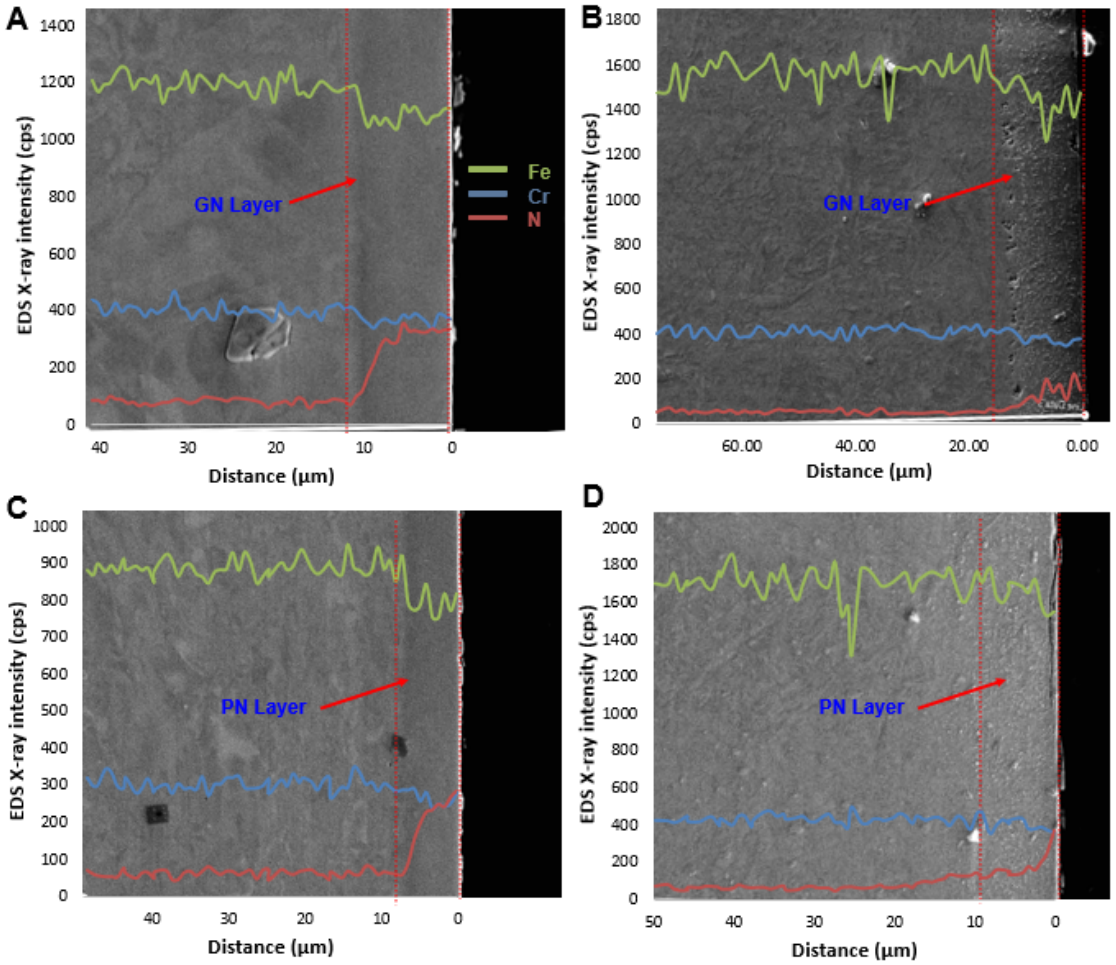

Figure 5.5: EDS line scan across the nitrided layer of GN and PN treated steels. (A) Gas nitrided 3015 alloy, (B) Gas nitrided X45CrSi9-3 steel, (C) Plasma nitrided 3015 alloy, (D) Plasma nitrided X45CrSi9-3 steel.

To further evaluate the spatial uniformity of nitriding over the valve head, the nitrided-layer thickness was examined at two additional locations. The locations are shown schematically in Fig 5.6 (A) and Fig 5.6 (B), respectively. The thickness obtained by gas nitriding produced a uniform nitriding layer of approximately 12.6 μm at both the valve face and valve bottom (Fig 5.6 (C) and Fig 5.6 (D)), consistent with that observed on the 3015 alloy part of the valve stem. This uniformity arises because gas nitriding can effectively treat the entire component, including the inner surfaces of holes and bores, representing a key advantage of the process. By contrast, plasma nitriding produced a much thinner nitriding layer of around 4.4μm at the valve face (Fig 5.6 (E)) and no measurable nitriding layer at the valve

bottom (Fig 5.6 (F)). This non-uniform nitriding behavior is attributed to the uneven plasma density over curved and recessed surfaces. Because nitrogen activation during plasma nitriding relies on glow-discharge ion bombardment, the process is sensitive to local conditions [44].

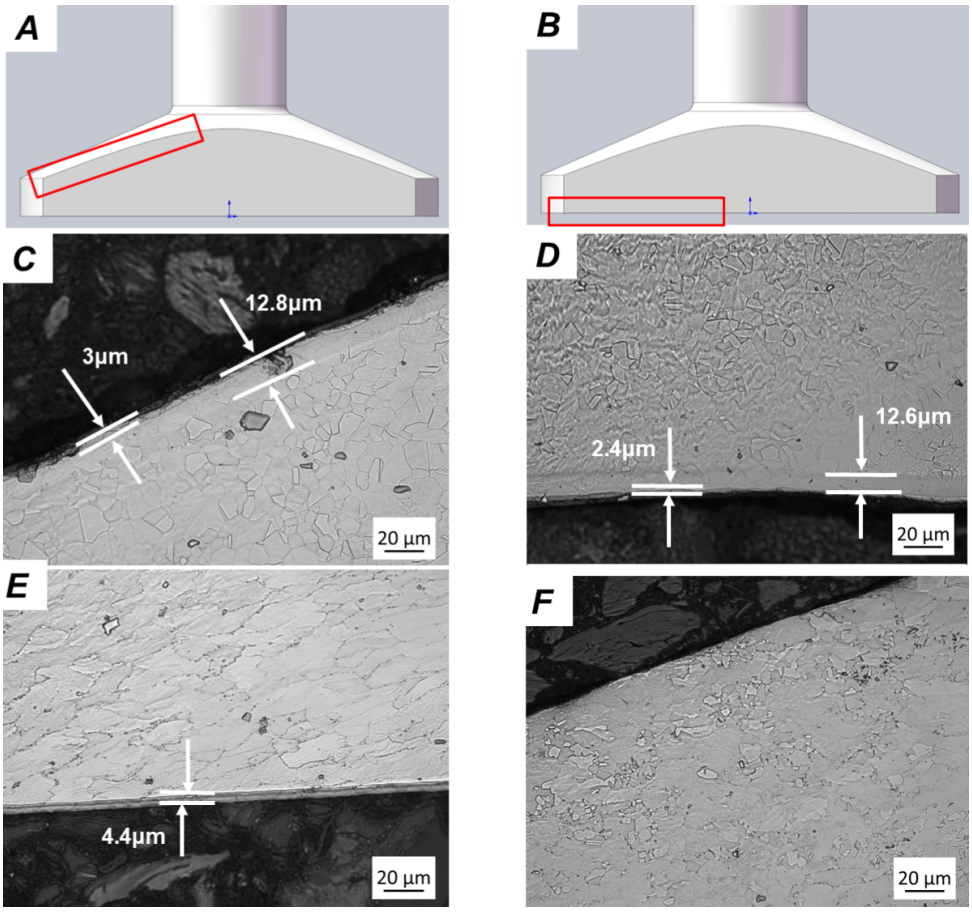

Figure 5.6: Microstructure of valve head after gas and plasma nitriding. Schematic imaging locations are given in (A) for the valve face and (B) for the valve bottom. (C, D) Gas nitrided valve face and bottom; (E, F) Plasma nitrided valve face and bottom.

5.1.2 Re-Nitrided Samples by Gas Nitriding in Bodycote

The tensile test specimens extracted from the 3015 alloy part and X45CrSi9-3 part in the valve stem using the EDM method were sent to Bodycote for renitriding. The detailed specimen geometry and gas nitriding process parameters are described in the method chapter. To investigate the microstructure and hardness of the specimen, the grip section of an untested nitrided tensile test bar was cut (Fig. 5.7 (A)). As shown in Fig. 5.7(B), the micro-Vickers hardness under a 100 gf load for the gas-nitrided specimen is much higher than that of the unnitrided specimen throughout the whole thickness. For the unnitrided tensile test specimen, the micro-hardness is approximately 300 HV, whereas the gas-nitrided specimen shows a value above 750 HV. As shown in Fig. 5.7 (C-E), it is hard to distinguish the nitrided layer from

the base material. Combining the micro-hardness, LOM, and tensile test results in section 5.3.2, it can be estimated that the 0.9 mm thick small X45CrSi9-3 tensile test specimen was fully gas nitrided. This extremely thick nitrided layer alters the material's mechanical properties, leading to the loss of almost plasticity during the slow-strain-rate tensile test. To avoid a similar problem, gas nitriding process parameters must be optimized for specific materials with specific geometries.

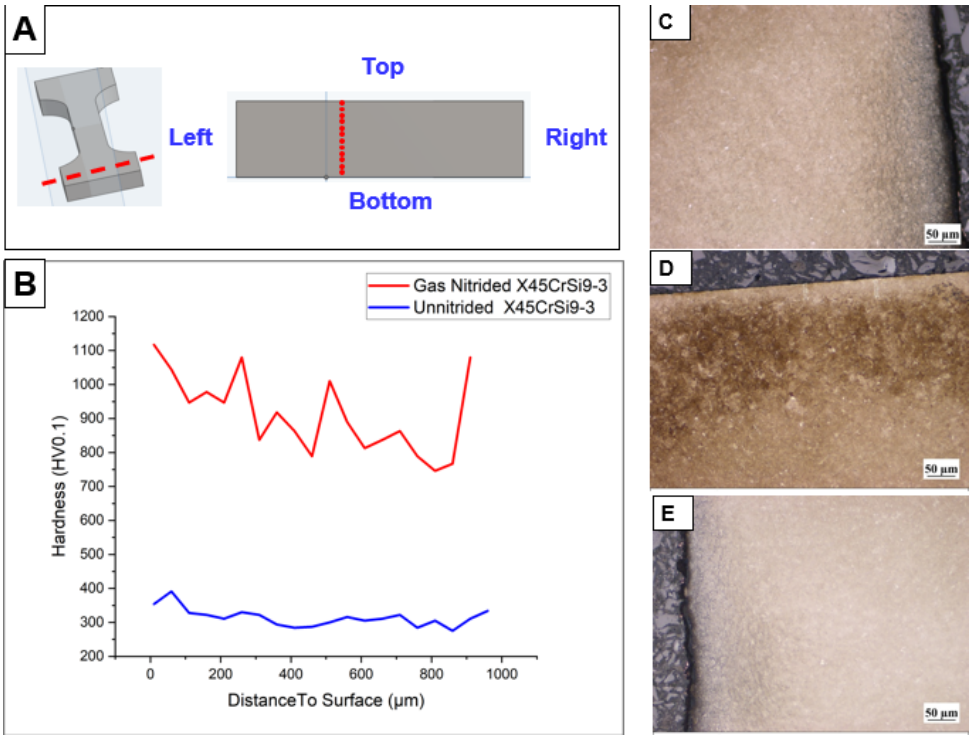

Figure 5.7: Microstructure and hardness profile of gas nitrided X45CrSi9-3: (A) Schematic of the tensile-test specimen, showing the cutting location (red dashed line) and vickers hardness test locations (red dots); (B) Vickers microhardness profile (HV0.1) for nitrided (red) and unnitrided (blue) steels from the grip section of the tensile specimen; (C) LOM image for right surface in A, (D) LOM image for top surface in A, (E) LOM image for left surface in A

Fig. 5.8 shows the microstructure and Vickers microhardness results of the gas nitrided 3015 alloy specimen. Unlike X45CrSi9-3 specimens, the right, top and left surfaces of this specimen are uniformly nitrided, and the nitriding layer thicknesses are between 24-38 μm. The case depth on the left and right surfaces (Fig. 5.8(C, D)) is larger than that on the top surface (Fig. 5.8(E)). This difference might be attributed to the different surface roughness between the EDM and ground surfaces. Notice that the tensile test samples were extracted from the engine valve using the EDM method. Afterwards, the top and bottom surfaces were ground with #2000-grit SiC paper to match the condition of the as-received engine valve, which was machined to 10μm surface roughness before nitriding. However, the left and right EDM surfaces (see Fig. 5.7 (A)) were not ground before being sent to Bodycote for re-nitriding due to the small dimensions of the tensile test specimens. In addition, as shown in Fig. 5.8(F), there is no nitrided layer observed at the bottom surface.

In theory, compared with plasma nitriding, gas nitriding is more uniform and can fully cover the component because it does not rely on glow-discharge ions, allowing the gas to be more evenly distributed in the atmosphere. However, both the 3015 alloy and X45CrSi9-3 steel are high-chromium materials, and the formation of a non-uniform nitriding layer after gas nitriding may be related to variations in the surface chromium oxide film, which can act as a barrier to nitrogen ingress during gas nitriding. Note that EDM involves localized melting and vaporization, whereas grinding induces plastic deformation, cutting, and abrasion. Likely, there exists a difference in the oxide film on different surfaces, in terms of thickness, chemistry, and defect density, etc. Consequently, the local ease of oxide film disruption or nitrogen penetration may vary across the surface, resulting in a non-uniform nitriding depth.

The Vickers microhardness result (Fig 5.8(B)) also confirms the LOM observation. For the left, top, and right surfaces, the microhardness near the surface is around 1400 HV, which is typical of the hardness of the gas-nitriding layer. As the distance from the surface increases, the hardness decreases and approaches the bulk hardness. For the bottom surface, the microhardness remains relatively constant throughout the thickness, at around 500 HV.

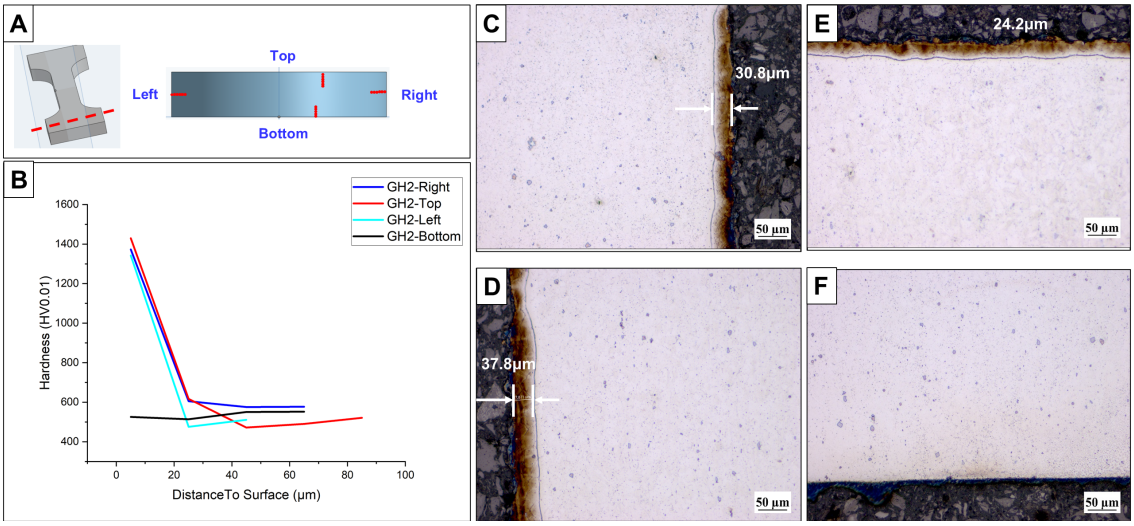

Figure 5.8: Microstructure and hardness profile of gas nitrided 3015 alloy: (A) Schematic of the tensile-test specimen, showing the cutting location (red dashed line) and Vickers hardness test locations (red dots); (B) Vickers microhardness profile (HV0.01) for all surfaces of the nitrided steel from grip section of tensile specimen; (C) LOM image for right surface in A; (D) LOM image for Top surface in A; (E) LOM image for left surface in A; (f) LOM image for bottom surface in A.

5.2 Hydrogen Content analysis

5.2.1 As-Received Engine Valve Materials

Hydrogen solubility and diffusion are key parameters for studying hydrogen embrittlement. To investigate hydrogen uptake, galvanostatic hydrogen pre-charging

was performed on as-received engine valve materials, followed by thermal desorption spectroscopy (TDS) measurement. To quantify hydrogen uptake in the two valve stem materials (3015 alloy and X45CrSi9-3 steel), the total hydrogen content under uncharged conditions was also measured using the Bruker G8 GALILEO ONH analyzer, which employs inert gas fusion technology. Three samples were tested in each condition for data reliability, and the average result was reported in Fig. 5.9(A). The engine valve received from TRATON and investigated in this study had undergone two different nitriding processes: gas nitriding and plasma nitriding. As shown in Fig. 5.9(A), the average total hydrogen content for gas-nitrided 3015 alloy is around 1.98 ppm, while the value for the other conditions is below 0.32 ppm. One possible explanation is that some of the hydrogen released from the ammonia dissociation reaction (Eq 2.1, Eq . 2.2) during the gas nitriding process may have entered the 3015 alloy material. Ojasalo et al. [47] reported similar results. When conducting 1000h gas nitriding on X40CrSiMo10-2 materials, the TDS results show that the hydrogen content is over 20 ppm, which is almost 7 times higher than that of the 100h gas nitriding process. For other materials, such as 316plus, the hydrogen content measured by TDS did not change significantly with different gas nitriding durations. This indicates that hydrogen trapping in the nitriding layer is governed by both the nitriding process parameters and the material microstructure. This may explain why approximately 2 ppm of hydrogen is found in the 3015 alloy, whereas only 0.22 ppm is found in X45CrSi9-3 steel.
The TDS analysis on the gas nitrided 3015 alloy shows that the hydrogen desorption peaks appear at approximately 780 °C (Fig. 5.9(B)), which is significantly higher than those trapped in bulk materials (255–339°C, Fig. 5.10(A)). This indicates that after gas nitriding, some hydrogen may be trapped in the dense nitriding layer or at interfaces associated with the nitriding layer. An earlier study by Zakroczymski et al. showed that the plasma-nitriding layer in austenitic steel can trap hydrogen and act as a hydrogen permeation barrier [48].

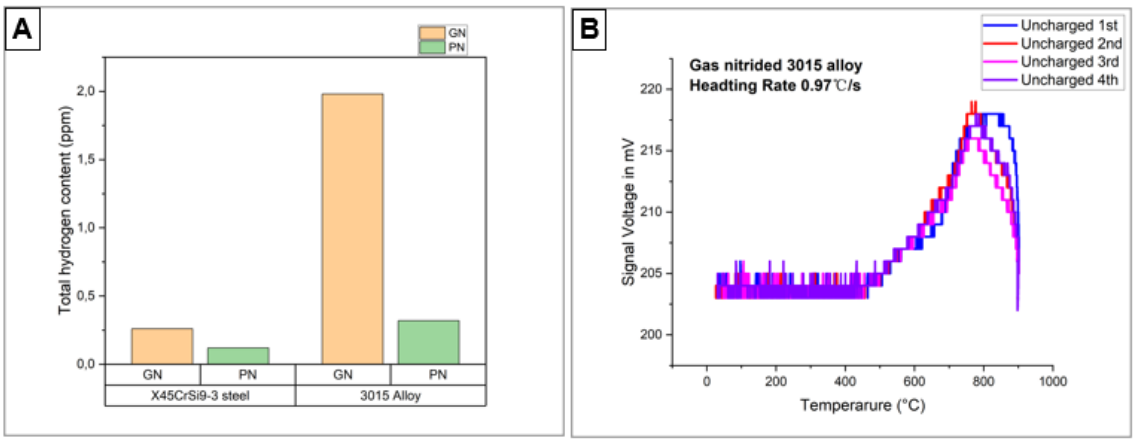

Figure 5.9: (A) Total hydrogen content for 3015 alloy and X45CrSi9-3 steel under uncharged conditions. (B) Thermal desorption curve obtained based on carrier gas hot extraction for gas nitrided 3015 alloy under uncharged conditions.

5.2.2 Hydrogen Charged Engine Valve Materials

When charging hydrogen electrochemically, its uptake is a function of electrolyte, temperature, charging time and temperature etc. In this study, 0.5 M H_2SO_4 and 3 g/L NH_4SCN were used as the electrolyte. The hydrogen content in the charged specimens was measured by the carrier-gas hot-extraction method. As expected, hydrogen uptake increased with increasing charging time and temperature, as seen in Fig. 5.10. At 52 °C, the hydrogen content in X45CrSi9-3 steel increased from 2.69 ppm after 4 h of charging to 10.01 ppm after 24 h. For a constant charging time of 4 h, increasing the charging temperature from 52 °C to 80 °C resulted in an increase in hydrogen content from 2.69 ppm to 6.48 ppm. This temperature dependence can be attributed to the temperature-dependent nature of hydrogen diffusion (Eq. 3.9). As the charging temperature increases, the hydrogen diffusion coefficient increases, facilitating faster hydrogen transport into the steel, consequently leading to a higher hydrogen uptake. For the 3015 alloy, similarly, the hydrogen content increased from 4.40 ppm after charging at 52 °C for 4 h to 20.47 ppm after charging at 80 °C for 24 h. Compared with X45CrSi9-3 steel, the austenitic 3015 alloy exhibited a higher hydrogen uptake at 52 °C for 4 h. The hydrogen content of the 3015 alloy reached 4.40 ppm, which is approximately 1.6 times that of X45CrSi9-3 steel (2.69 ppm). This higher hydrogen uptake can be attributed to the higher hydrogen solubility of the austenitic structure. Although the lower diffusivity limits the rate of hydrogen transport, the higher solubility enables the austenitic alloy to retain a greater amount of hydrogen.

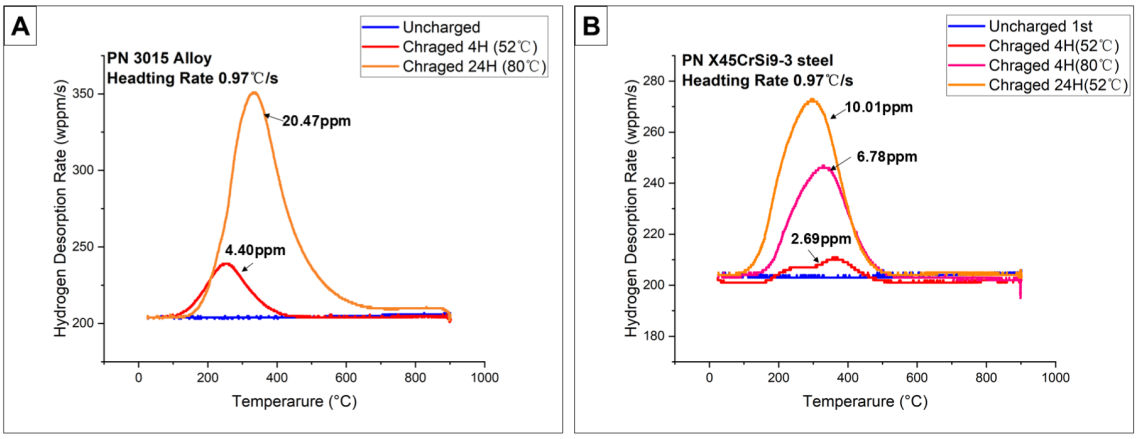

Figure 5.10: Hydrogen content obtained by carrier gas hot extraction for plasma nitrided 3015 alloy (A) and X45CrSi9-3 steel (B), charged in 0.5 M H_2SO_4 + 3 g/L NH_4SCN electrolyte.

5.3 Mechanical Properties

5.3.1 Tensile Stress-Strain Responses

5.3.1.1 X45CrSi9-3 Steel in the Valve Stem

The slow strain rate tensile test was conducted at a strain rate of $1 \times 10^{-4} s^{-}$ to evaluate the hydrogen embrittlement susceptibility for valve stem X45CrSi9-3 material. The results are shown in Fig. 5.11. Table 5.1 summarizes the mechanical properties including ultimate tensile strength (R_m), yield strength($R_{p0.2}$), total elongation(δ), reduction of area(φ), and hydrogen embrittlement index (HEI) for unnitrided X45CrSi9-3 specimens without and with hydrogen charging. Hydrogen charging was performed at different current densities and charging times using sulfuric acid solutions of different molar concentrations, with 3 g/L NH_4SCN added as a poison to prevent recombination of hydrogen protons, at different charging currents and charging times. The blue line in Fig. 5.11 confirms that X45CrSi9-3 material under hydrogen-free conditions possesses good strength and outstanding ductility. The tensile strength and total elongation are 1253.8 MPa and 18.4%, respectively. However, with hydrogen charging, changes in material strength and ductility are observed, even after only 2 hours of charging (black line in Fig. 5.11). The total elongation is around 6.4%, and the hydrogen embrittlement index calculated using equation 4.2 is 65%. When charging in 0.5 M H_2SO_4 solution for 18 h at a current density of 30 mA/cm^2, the specimen shows the lowest strength with an ultimate tensile strength of only 940.4 MPa (the origin line in Fig. 5.11). The ductility is lost almost completely.

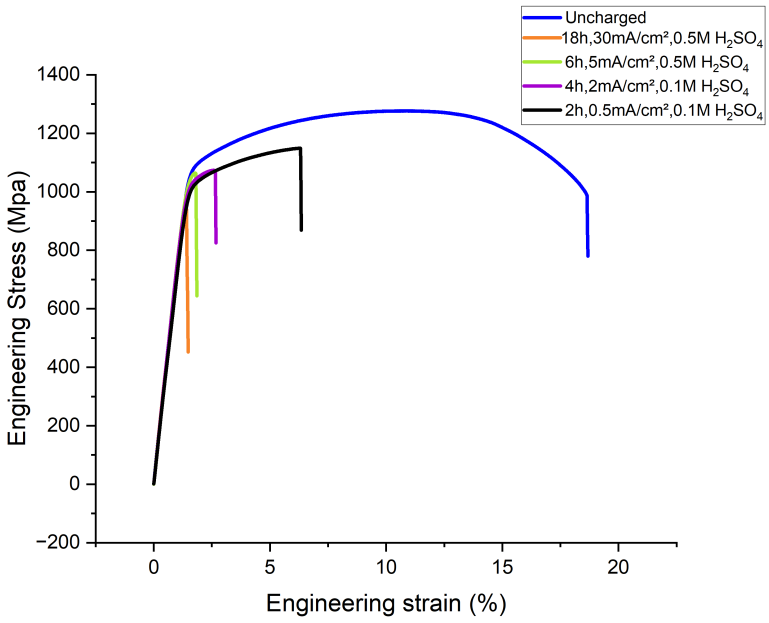

Figure 5.11: Tensile curves of as-received X45CrSi9-3 at different conditions of electrochemical hydrogen charging

When the charging time is reduced to 6 hours and the charging current density to 5 mA/cm^2 (green line in Fig 5.11), the ultimate tensile strength increases to 1063.7 MPa, while the yield strength remains comparable to that of the uncharged condition. However, the specimen still exhibits very low elongation after fracture. Obviously, charging conditions affect mechanical properties significantly. Reducing charging time, current density, and sulfuric acid concentration lower electrochemical charging efficiency and consequently hydrogen uptake, increasing the elongation of the specimen.

Table 5.1: Mechanical properties of unnitrided X45CrSi9-3 specimen with and without hydrogen charging.

Charging conditions	R_m(MPa)	$R_{p0.2}$(MPa)	δ(%)	φ(%)	HEI(%)
Uncharged	1253.8	1041.7	18.4	11	–
18h,30 mA/cm^2, 0.5 M H_2SO_4	940.4	894.3	1.5	3	91.8
6h,5 mA/cm^2, 0.5 M H_2SO_4	1063.7	1045.1	1.9	2	89.7
4h,2 mA/cm^2, 0.1 M H_2SO_4	1073.5	1014.5	2.7	4	85.3
2h,0.5 mA/cm^2, 0.1 M H_2SO_4	1149.1	1008.3	6.4	5	65.2

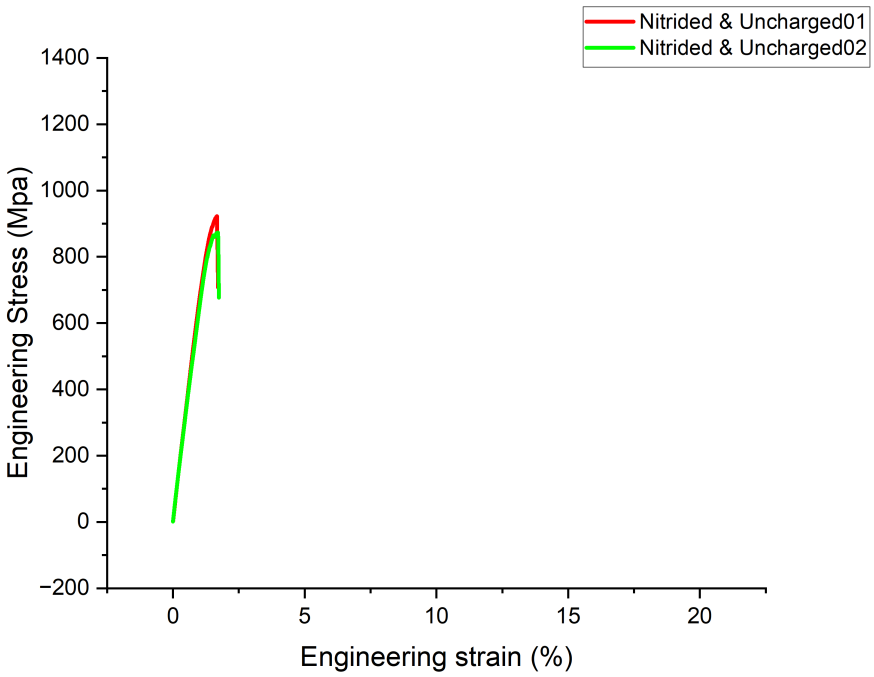

Figure 5.12: Tensile curves of X45CrSi9-3 re-nitrided in Bodycote without hydrogen charging

Figure 5.12 shows the slow strain rate tensile curves for re-nitrided X45CrSi9-3 specimens without hydrogen charging. Table 5.2 summarize the mechanical properties including ultimate tensile strength (R_m), yield strength($R_{p0.2}$), total elongation(δ),

and reduction of area(φ). From the results, it can be seen that re-nitrided X45CrSi9-3 exhibits poor strength and extremely low ductility even under uncharged conditions. This can be explained as follows. The small thickness of the tensile specimens (0.9 mm) enables complete nitriding throughout the entire thickness, as confirmed by the detailed microstructural analysis presented in Chapter 5.1, resulting in high brittleness.

Table 5.2: Mechanical properties of X45CrSi9-3 re-nitrided in Bodycote without hydrogen charging.

Charging conditions	R_m(MPa)	$R_{p0.2}$(MPa)	δ(%)	φ(%)
Uncharged-1	922.6	901.1	1.7	0.5
Uncharged-2	873.5	862.3	1.7	2.4

5.3.1.2 3015 Alloy in the Valve Stem

Figure 5.13 shows the tensile curves of the unnitrided 3015 alloy specimens from the valve stem. Table 5.3 summarizes the detailed mechanical properties. For the uncharged conditions, two specimens were tested, as shown in Fig. 5.13 (a). The results show a slight difference in their mechanical properties. Specimen 2 exhibited the higher ultimate tensile strength, with a value of 1469.3 MPa, compared with approximately 1431.2 MPa for specimen 1. The elongation also differed by approximately 2.5% between the two specimens. These differences indicate that some microstructural variation might exist between tensile specimens extracted from the 3015 alloy part in the valve stem, even when they are taken from closely adjacent areas. Due to time limitations, detailed differences in microstructure were not examined in this study and will be investigated in future studies. For HE studies, specimen 1 was selected as the baseline condition.

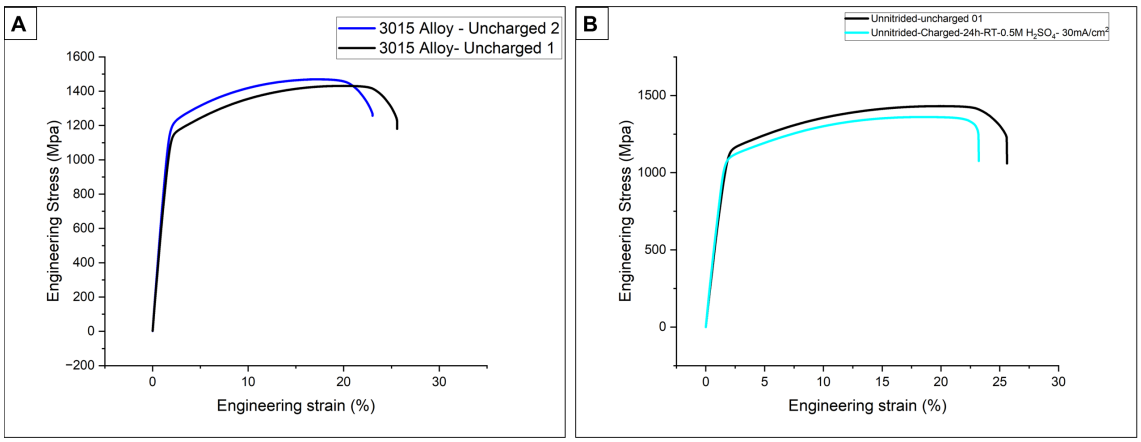

Figure 5.13: Tensile curves of unnitrided 3015 alloy. (A) Uncharged samples, (B) Comparison of charged and uncharged samples

Table 5.3: Mechanical properties of unnitrided 3015 alloy.

Charging conditions	R_m(MPa)	$R_{p0.2}$(MPa)	δ(%)	φ(%)	HEI(%)
Uncharged-1	1431.2	1077.8	25.6	19.2	–
Uncharged-2	1469.3	1142.6	23.1	17.3	–
Charged, 24h, RT, 30 mA/cm^2, 0.5 M H_2SO_4	1360.7	1055.7	23.4	19.1	8.6

Figure 5.13 (b) compares the unnitrided 3015 alloy under charged and uncharged conditions. The HEI after charging at room temperature for 24 h was 8.6%, which is much lower than that of the X45CrSi9-3 material. This indicates a large difference in HE susceptibility between austenitic and ferritic/martensitic stainless steels. The 3015 alloy has an FCC austenitic structure. The hydrogen diffusion coefficient at room temperature is reported to be extremely slow ($\sim 10^{-12} cm^2/s$). It is approximately seven orders of magnitude lower than in BCC ferrite/martensite ($\sim 10^{-5} cm^2/s$) [49]. This means that hydrogen migration in the austenitic 3015 alloy is much slower than in the martensitic X45CrSi9-3 alloy. Conversely, austenitic steel exhibits significantly higher hydrogen solubility due to the larger octahedral interstitial sites available in the FCC lattice [50], allowing more hydrogen to be stored in the austenitic structure but less transported. These contrasting properties have direct implications for hydrogen embrittlement susceptibility. In the martensitic X45CrSi9-3 specimen, hydrogen accumulates rapidly and results in higher susceptibility to hydrogen embrittlement, while the austenitic 3015 alloy may accumulate larger hydrogen content under prolonged charging time despite its lower diffusion kinetics. Nevertheless, the 3015 alloy was less susceptible to hydrogen embrittlement than the X45CrSi9-3 steel under the investigated condition.

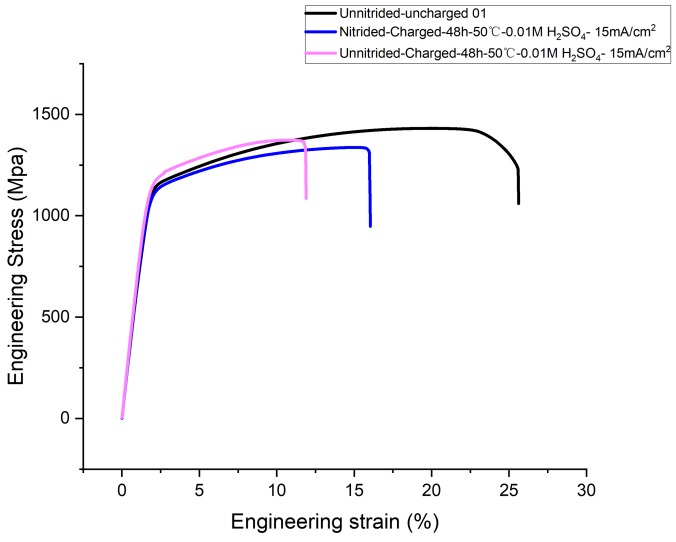

Figure 5.14: Tensile curves of the 3015 alloy re-nitrided in Bodycote

Table 5.4: Mechanical properties of nitrided and unnitrided 3015 alloy under different charging conditions.

Charging conditions	R_m(MPa)	$R_{p0.2}$(MPa)	δ(%)	φ(%)	HEI(%)
Unnitrided-uncharged-1	1431.2	1077.8	25.6	19.2	–
Nitrided, 48h, 50℃, 15 mA/cm^2, 0.01 M H_2SO_4	1336.8	1027.8	16	6.4	37.5
Unnitrided, 48h, 50℃, 15 mA/cm^2, 0.01 M H_2SO_4	1373	1091.2	11.9	10.6	53.5

The slow strain rate tensile test was also conducted for gas nitrided 3015 alloy specimens, as shown in Fig. 5.14. The detailed mechanical properties are listed in Table 5.4. When the unnitrided 3015 alloy is charged for 48 hours in the given condition (Magenta curve in Fig. 5.14), its ductility is reduced significantly. The total elongation decreased to only 11.9%, which is less than half that of the uncharged sample. In comparison, the nitrided sample charged in the same condition has a higher elongation of 16% (Blue curve in Fig. 5.14), implying a beneficial effect of nitriding on HE resistance. Note that, as revealed in Chapter 5.1, nitrided layers were observed on only three surfaces of this batch of 3015 alloy, which is assumed to reduce the protective effect of the nitriding layer.

5.3.2 Fractography

Figure 5.15 shows the fracture surface of specimens tested by SSRT under hydrogen-free conditions. The nitrided X45CrSi9-3 steels (Fig. 5.15 (A)) exhibit a typical brittle fracture surface, with little or no necking. Near the edge of the fracture surface (Fig 5.16 (A′)), intergranular-like fracture features was also observed, together with approximately 200 μm thick flat regions. This is consistent with the significant reduction in elongation after re-nitriding, from 18.4% for unnitrided X45CrSi9-3 to 1.7% for re-nitrided specimens. Previous OM, EDS, and microhardness results indicate excessive nitrogen penetration through the specimen cross section. This may contribute to severe loss in material ductility, even without hydrogen pre-charging. By contrast, the unnitrided X45CrSi9-3 steels show a typical ductile fracture with clear necking (Fig. 5.15 (C)) and small dimples in the magnified images (Fig 5.16 C′). This indicates substantial plastic deformation before fracture. Fig. 5.15 (B) and (D) present the fracture surfaces of nitrided and unnitrided 3015, respectively. Both specimens show predominantly ductile fracture, however, a thin, flat area was visible at the edge of the nitrided 3015 (Fig 5.16 B′). This region is suggested to result from gas nitriding and the high N content at the surface, which may promote the formation of this brittle layer. Compared with the nitrided X45CrSi9-3, however, this layer is approximately 40% as thick. Typical dimples were also observed in nitrided and unnitrided 3015 alloys (Fig 5.16 B′, Fig 5.16 D′).

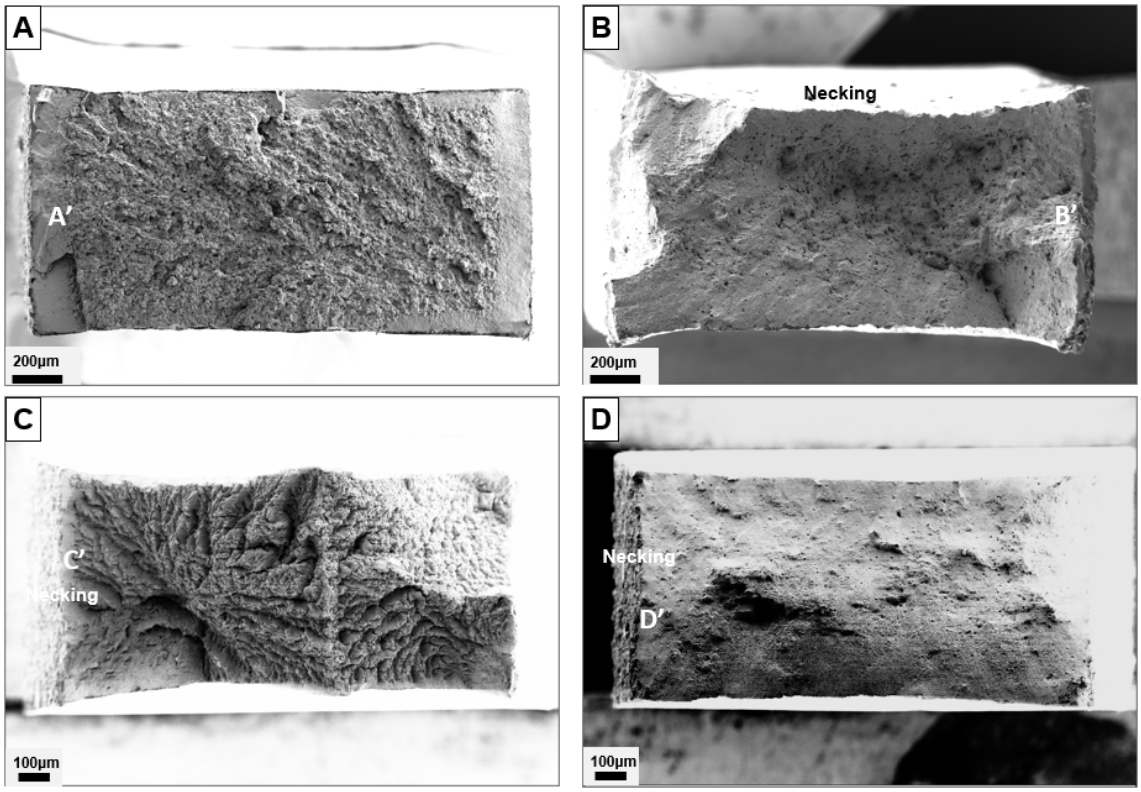

Figure 5.15: SEM images of the fracture surfaces of hydrogen-free tensile specimens: (A) Gas nitrided X45CrSi9-3, (B) Gas nitrided 3015, (C) Unnitrided X45CrSi9-3, (D) Unnitrided 3015.

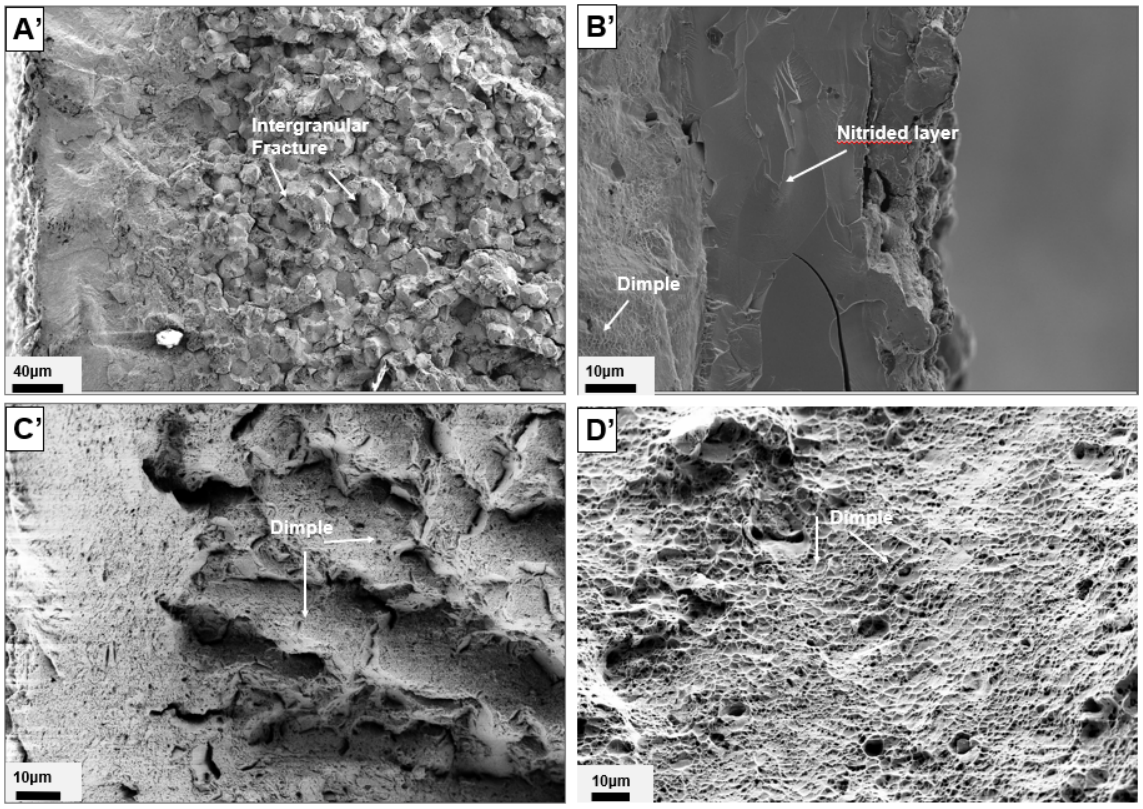

Figure 5.16: Magnified images from the fracture surfaces in Fig.5.15. (A′) region A′ in Fig.5.15, (B′) region B′ in Fig.5.15, (C′) region C′ in Fig.5.15, (D′) region D′ in Fig.5.15.

The fracture surfaces after SSRT of the nitrided and unnitrided 3015 alloys, charged under the same conditions, were also examined by SEM. Both specimens were charged for 48 hours in 0.01 M H_2SO_4 + 3g/L NH_4SCN electrolyte at50 °C and 15 mA/cm^2 prior to tensile tests. As shown in Fig. 5.17 (A and E), the overall fracture mode is ductile for both samples, as evidenced by clear necking and the presence of dimples in the magnified images. A hydrogen-affected zone is observed near the specimen edge. However, the nitrided specimen exhibits a much smaller hydrogen-affected zone than the unnitrided specimen. The brittle-appearing fracture region is only around 16.2 μm thick (Fig. 5.17 (B)) in the nitrided 3015 specimen. The high-magnification image in Fig. 5.17 (D) reveals the mixed fracture morphology, including both typical ductile dimples and relatively flat facets with river-pattern-like markings. In contrast, the near-surface regions with brittle-appearing fracture features in unnitrided 3015 extended approximately 46 μm thick from both the top and bottom surfaces (Fig. 5.17 (F and G)). The higher magnification image in Fig. 5.17 (H) reveals the typical cleavage with step-like and locally river-like markings, indicating a locally brittle fracture morphology.
Compared with the unnitrided specimen, the nitrided 3015 specimen exhibits a narrower near-surface region with brittle fracture features. These observations suggest that the nitriding layer possibly modifies the surface response to hydrogen and helps to restrict the development of the brittle hydrogen-affected zone. This is consistent with the observations in the SSRT results.

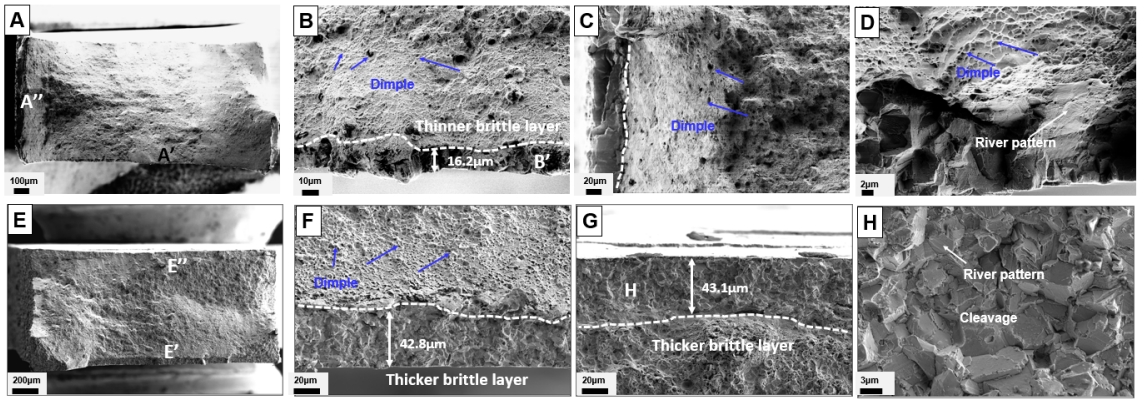

Figure 5.17: SEM images of the fracture surfaces after SSRT from the nitrided (A-D) and unnitrided (E-H) 3015 alloys, charged at50 $°C$ and 15mA/cm^2 current density in 0.01M H_2SO_4 + 3g/L NH_4SCN electrolyte for 48h prior to tensile tests. (A) Fracture surface of nitride 3015, (B) region A′ in (A), (C) region A″ in (A), (D) magnified image of B′ in (B); (E) fracture surface of unnitrided 3015, (F) region E′ in (E), (G) E″ in (E), (H) magnified image of (G).

The fracture surface after SSRT of the nitrided and unnitrided X45CrSi9-3 steel with charged hydrogen was also examined to evaluate the susceptibility to HE. Hydrogen precharging was performed at RT for 2 h in a 0.1 M H_2SO_4 + 3 g/L NH_4SCN electrolyte at a current density of 0.5 mA/cm^2. As shown in Fig. 5.18(A), the fracture surface of unnitrided X45CrSi9-3 exhibits a rough, irregular morphology. At higher magnification, irregular facets were also observed in the edge section (Fig. 5.18(B)). In the center section, localized dimple-like and tearing features were observed (Fig. 5.18(C)). This fractography result suggests that the fracture morphology combines brittle-like and ductile fracture characteristics. In this hydrogen precharging and SSRT condition, the specimen's elongation decreases from 18.4% in the uncharged condition to 6.4% after hydrogen exposure, indicating a significant loss in ductility. For the nitrided specimen, the fracture surface exhibits a relatively flat profile with little or no necking (Fig. 5.18(D)). A flat region was also observed near the edge region, while the center region shows rougher morphology (Fig. 5.18(E)). In a higher-magnification image of the center section, irregular facets and tearing-like features were also observed (Fig. 5.18(F)). Similar fracture morphology was also found in the nitrided X45CrSi9-3 specimen under hydrogen-free conditions, especially in the flat edge region. As discussed before, an excessive nitriding layer already caused significant loss of elongation, from 18.4% to 1.7%, under hydrogen-free conditions. So, the brittle fracture behavior cannot be attributed solely to hydrogen. From the current SEM observations, no clear additional changes in fracture morphology could be distinguished.

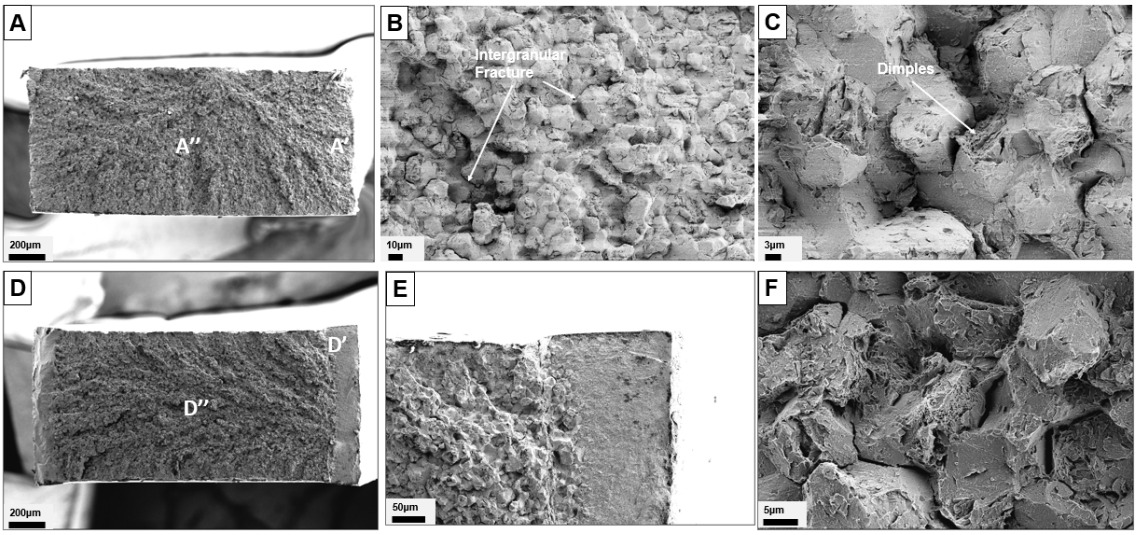

Figure 5.18: SEM images of the fracture surfaces after SSRT from the unnitrided (A–C) and nitrided (D–F) X45CrSi9-3 steel in 0.1 M H_2SO_4 + 3g/L NH_4SCN electrolyte for 2 h at RT using a current density of 0.5mA/cm^2 prior to the tensile test. (A, D) Overview of the fracture surface, (B) magnified images of A′ in (A), (C) magnified images of A″ in (A),(E) magnified images of D′ in (D), (F) magnified images of D″ in (D).

6

Conclusions

This thesis investigates nitriding as a potential alternative to conventional chromium electroplating using carcinogenic Cr(VI) compounds for engine valves used in a hydrogen internal combustion engine. The study evaluates both as-received engine valves subjected to gas and plasma nitriding, as well as re-nitrided tensile test specimens by gas nitriding in Bodycote. Based on the results presented in this thesis, the main conclusions are as follows.

As received engine valves

1. Both gas nitriding and plasma nitriding in as-received engine valves form nitrided surface layers. However, the gas nitrided layer is generally thicker and more uniform, while the plasma nitrided layer is thinner and its distribution is more influenced by the valve geometry.
2. Under the same nitriding conditions, the nitrided layer thicknesses differ between 3015 and X45CrSi9-3, which can be attributed to differences in microstructure, N diffusion behavior, and Cr content. In the BCC martensitic X45CrSi9-3, N diffusion is faster, while the FCC structure of 3015 is more restrictive to N diffusion. Furthermore, Cr has a higher affinity for N, which further limits N penetration during nitriding.
3. Hydrogen content analysis by TDS and inert gas fusion shows that 3015 has a higher hydrogen absorption capacity than X45CrSi9-3. The gas nitriding process may also introduce hydrogen into the material, especially in the 3015 alloy. Hydrogen trapped in the nitriding layer has a higher desorption temperature than hydrogen trapped in the bulk material.

Re-nitrided tensile test samples in Bodycote

1. X45CrSi9-3 tensile specimens were fully nitrided, resulting in a significant reduction in plasticity even under hydrogen-free conditions. This indicates that the nitriding process needs to be optimized according to the specimen geometry and materials, especially for high Cr alloys.
2. Uneven nitrided layers were observed on the 3015 alloy tensile specimens. The high Cr content makes gas nitriding more challenging. Optimization of the process parameters of nitriding or the use of additional pre-treatment is required to improve nitriding efficiency and layer uniformity.
3. In the unnitrided condition, hydrogen charging causes a more pronounced reduction in the strength and ductility of X45CrSi9-3 than in 3015 alloy, indicating that X45CrSi9-3 is more susceptible to HE. Although 3015 exhibits lower susceptibility, an obvious sign of HE is still observed after hydrogen charging at elevated temperature.
4. In the same charging condition, the nitrided 3015 alloy has a higher total elonga-

tion (16%) than the unnitrided specimen (11.9%), despite only three surfaces being nitrided. This indicates that nitriding has the potential to improve the hydrogen tolerance of 3015.
5. Fractography analysis shows that the unnitrided samples exhibit a wider hydrogen-affected zone and more pronounced river pattern, while the hydrogen-affected region in the nitrided sample is thinner, indicating that the nitriding layer has a certain limiting effect on HE.
However, this study has some limitations. Laboratory tests cannot fully represent actual hydrogen internal combustion engine operating conditions, where valves are exposed to varying temperatures, hydrogen gas pressures, and mechanical stresses. In addition, electrochemical hydrogen charging differs from hydrogen exposure in a gaseous environment. Therefore, further investigations under more representative operating conditions are needed to evaluate the long-term performance of nitrided valves.

7
Future plan

Based on the present results, several interesting topics remain to be investigated to further clarify the role of the nitriding layer in the HE susceptibility of engine valve materials.
First, additional studies on plasma nitriding should be conducted, since the current study primarily focuses on gas nitriding. Plasma nitriding may be more suitable for high Cr material, because sputtering during the process can remove the chromium oxide layer from the material surface, facilitating nitriding. Therefore, it would be valuable to compare the hardness, hydrogen uptake, and fracture behavior of plasma-nitrided and unnitrided specimens under the same charging conditions.
Second, bending test should be performed to evaluate the mechanical response of the nitriding layer. Since engine valves may experience complex stress states during operation, bending tests can provide complementary information to SSRT and may help determine whether the nitriding layer can reduce hydrogen-induced mechanical degradation and improve the materials' resistance to hydrogen-induced cracking during service relevant conditions.
Further studies on nitriding parameters, hydrogen trapping behavior and optimization of nitride layer thickness are also needed. In particular, the relationship between nitriding conditions, layer characteristics, hydrogen uptake, and HE resistance should be systematically investigated to identify optimized nitriding parameters for engine valve materials operating under hydrogen-rich environments.

Bibliography

[1] OOZX Corporation, "Engine Valve Technology," OOZX Corporation. [Online]. Available: https://www.oozx.co.jp/en/technology/valve/. [Accessed: May 31, 2026].

[2] A. Mehtab, S. A. Ali, I. Sadiq, S. Shaheen, H. Khan, M. Fazil, N. A. Pandit, F. Naaz, and T. Ahmad, "Hydrogen Energy as Sustainable Energy Resource for Carbon-Neutrality Realization," *ACS Sustainable Resource Management*, vol. 1, no. 4, pp. 604–620, 2024. DOI: 10.1021/acssusresmgt.4c00039

[3] I. M. Robertson, P. Sofronis, A. Nagao *et al.*, "Hydrogen Embrittlement Understood," *Metallurgical and Materials Transactions A*, vol. 46, pp. 2323–2341, 2015. DOI: https://doi.org/10.1007/s11661-015-2836-1

[4] Bayata, F. and Alpas, A. T. (2021) The high temperature wear mechanisms of iron-nickel steel (NCF 3015) and nickel based superalloy (Inconel 751) engine valves. *Wear*, 480–481, 203943. doi:10.1016/j.wear.2021.203943.

[5] European Chemicals Agency (ECHA) (n.d.) Completed activities on restriction. Available at: https://echa.europa.eu/completed-activities-on-restriction (Accessed: 21 April 2026).

[6] Cao, Y., Maistro, G., Norell, M., Pérez-Garcia, S. A. and Nyborg, L. (2014) Multi-technique characterization of low-temperature plasma nitrided austenitic AISI 304L and AISI 904L stainless steel. *Surface and Interface Analysis*, 46(10–11), 856–860. doi:10.1002/sia.5462.

[7] Carpenter Technology (2026) NCF 3015/30 Ni valve steel – specialty alloys. Available at: https://www.carpentertechnology.com/alloy-finder/ncf-301530-ni-valve-steel (Accessed: 24 March 2026).

[8] D. Pierce, A. Haynes, J. Hughes, R. Graves, P. Maziasz, G. Muralidharan, A. Shyam, B. Wang, R. England, and C. Daniel, "High temperature materials for heavy duty diesel engines: Historical and future trends," *Progress in Materials Science*, vol. 103, pp. 109–179, Jun. 2019, doi: 10.1016/j.pmatsci.2018.10.004.

[9] Nguyen Duong Nam, Nguyen Anh Xuan, Nguyen Van Bach, Le Thi Nhung and Le Thi Chieu (2019) Control gas nitriding process: a review. *Journal of Mechanical Engineering Research & Developments*, 42(1), 17–25. doi:10.26480/jmerd.01.2019.17.25.

[10] Yu-Long Zhou, Fan Xia, Ai-Jun Xie, Hao-Ping Peng, Jian-Hua Wang and Zhi-Wei Li (2023) A Review—Effect of Accelerating Methods on Gas Nitriding: Accelerating Mechanism, Nitriding Behavior, and Techno-Economic Analysis. *Coatings*, 13(11), 1846. doi:10.3390/coatings13111846.

[11] M. S. Alekseeva, M. A. Gress, S. P. Scherbakov, S. A. Gerasimov and L. I. Kuksenova (2017) The Influence of High-Pressure Gas Nitriding on the Properties of Martensitic Steels. *Metal Science and Heat Treatment*, 59, 524–528. doi.org/10.1007/s11041-017-0183-0

[12] S. K. Singh, Ch. Naveen, Y. Venkat Sai, U. Satish, Ch. Bandhavi and Ram Subbiah (2019) Experimental Study on Wear Resistance of AISI 347 Treated With Salt Bath Nitriding and Gas Nitriding Processes-A Review. *Materials Today: Proceedings*, 18(7), 2717–2722. doi:10.1016/j.matpr.2019.07.134.

[13] J. Michalski, P. Wach, J. Tacikowski, M. Betiuk, K. Burdynski, S. Kowalski and A. Nakonieczny (2009) Contemporary Industrial Application of Nitriding and Its Modifications. *Materials and Manufacturing Processes*, 24(7–8), 855–858. doi:10.1080/10426910902844203.

[14] T. Bell, K. Mao and Y. Sun (1998) Surface engineering design: modelling surface engineering systems for improved tribological performance. *Surface and Coatings Technology*, 108–109, 360–368. doi:10.1016/S0257-8972(98)00623-9.

[15] Li Yang, Liang Wang, Dandan Zhong and Lie Shen (2010) The effect of surface nanocrystallization on plasma nitriding behaviour of AISI 4140 steel. *Applied Surface Science*, 257, 979–984. doi:10.1016/j.apsusc.2010.08.004.

[16] W. Arabczyk and J. Zamlynny, "Study of the ammonia decomposition over iron catalysts," *Catalysis Letters*, vol. 60, no. 3, pp. 167–171, 1999. doi: 10.1023/A:1019007024041.

[17] J. H. Abboud, A. F. Fidel and K. Y. Benyounis (2008) Surface nitriding of Ti–6Al–4V alloy with a high power CO_2 laser. *Optics & Laser Technology*, 40(2), 405–414. doi:10.1016/j.optlastec.2007.07.005.

[18] Therelek (2026) Plasma nitriding process: an in-depth look. *Therelek*. Available at: `https://www.therelek.com/plasma-nitriding-process-an-in-depth-look/`.

[19] Prozesswaerme (2026) Plasma nitriding: the process and its advantages. *Prozesswaerme*. Available at: `https://prozesswaerme.net/heat-processing/plasma-nitriding-the-process-and-its-advantages/`.

[20] K. Ram Mohan Rao, K. Trinadh and C. Nouveau (2019) Glow discharge plasma nitriding of low alloy steel. *Materials Today: Proceedings*, 19, 864–866. doi:10.1016/j.matpr.2019.08.224.

[21] F. Bao, E. Kemppainen, I. Dorbandt, R. Bors, F. Xi, R. Schlatmann, R. van de Krol, and S. Calnan, "Understanding the Hydrogen Evolution Reaction Kinetics of Electrodeposited Nickel-Molybdenum in Acidic, Near-Neutral, and Alkaline Conditions," *ChemElectroChem*, vol. 8, no. 1, pp. 195–208, Jan. 2021, doi: 10.1002/celc.202001436.

[22] Johnson, W. H. (1875) II. On some remarkable changes produced in iron and steel by the action of hydrogen and acids. *Proceedings of the Royal Society of London*, 23, 168–179.

[23] Li, X., Ma, X., Zhang, J., Akiyama, E., Wang, Y. and Song, X. (2020) Review of hydrogen embrittlement in metals: hydrogen diffusion, hydrogen characterization, hydrogen embrittlement mechanism and prevention. *Acta Metallurgica Sinica (English Letters)*, 33(6), 759–773. doi:10.1007/s40195-020-01039-7.

[24] S. Pillot and L. Coudreuse, "Hydrogen-induced disbonding and embrittlement of steels used in petrochemical refining," in *Gaseous Hydrogen Embrittlement of Materials in Energy Technologies, Vol. 2: The Problem, its Characterisation and Effects on Particular Alloy Classes*, Woodhead Publishing Series in Metals and Surface Engineering, 2012, pp. 51–93, doi: 10.1533/9780857093899.1.51.

[25] Zapffe, C. A. and Sims, C. E. (1941) Hydrogen embrittlement, internal stress and defects in steel. *Trans. AIME*, 145, 225–271.

[26] Beachem, C. D. (1972) A new model for hydrogen-assisted cracking (hydrogen "embrittlement"). *Metallurgical Transactions*, 3(2), 441–455.

[27] Birnbaum, H. K. and Sofronis, P. (1994) Hydrogen-enhanced localized plasticity—a mechanism for hydrogen-related fracture. *Materials Science and Engineering A*, 176(1–2), 191–202.

[28] Ferreira, P. J., Robertson, I. M. and Birnbaum, H. K. (1998) Hydrogen effects on the interaction between dislocations. *Acta Materialia*, 46(5), 1749–1757.

[29] Matsumoto, T., Eastman, J. and Birnbaum, H. K. (1981) Direct observations of enhanced dislocation mobility due to hydrogen. *Scripta Metallurgica*, 15(9), 1033–1037.

[30] Pfeil, L. B. (1926) The effect of occluded hydrogen on the tensile strength of iron. *Proceedings of the Royal Society of London. Series A*, 112, 182–195.

[31] Li, Q., Ghadiani, H., Jalilvand, V., Alam, T., Farhat, Z. and Islam, M. A. (2024) Mechanisms of hydrogen embrittlement. In *Encyclopedia*. Available at: `https://encyclopedia.pub/entry/55571`.

[32] Martínez-Pañeda, E., del Busto, S., Niordson, C. F. and Betegón, C. (2016) Strain gradient plasticity modeling of hydrogen diffusion to the crack tip. *International Journal of Hydrogen Energy*, 41, 10265–10274.

[33] Katzarov, I. H. and Paxton, A. T. (2017) Hydrogen embrittlement II. Analysis of hydrogen-enhanced decohesion across (111) planes in α-Fe. *Physical Review Materials*, 1, 033603.

[34] Lynch, S. P. (1979) Hydrogen embrittlement and liquid-metal embrittlement in nickel single crystals. *Scripta Metallurgica*, 13, 1051–1056.

[35] Dwivedi, S. K. and Vishwakarma, M. (2018) Hydrogen embrittlement in different materials: a review. *International Journal of Hydrogen Energy*, 43, 21603–21616.

[36] Lynch, S. P. (2011) Hydrogen embrittlement (HE) phenomena and mechanisms. In *Gaseous Hydrogen Embrittlement of Materials in Energy Technologies, Volume 1: The Problem, Its Characterisation and Effects on Particular Alloy Classes and Hydrogen Systems*, pp. 90–130. doi:10.1533/9780857093769.1.90.

[37] Fountains of Bryn Mawr (2013) *Microscope compound diagram.* Wikimedia Commons. Available at: `https://commons.wikimedia.org/wiki/File:Microscope_compound_diagram.png` (Accessed: 31 March 2026). Licensed under CC BY-SA 3.0.

[38] M. Mazumder, R. Ahmed, A. W. Ali, and S.-J. Lee, "SEM and ESEM techniques used for analysis of asphalt binder and mixture: A state of the art review," *Construction and Building Materials*, vol. 186, pp. 313–329, Oct. 2018, doi: 10.1016/j.conbuildmat.2018.07.126.

[39] A. J. Wilkinson and T. B. Britton, "Strains, planes, and EBSD in materials science," *Materials Today*, vol. 15, no. 9, pp. 366–376, Sep. 2012, doi: 10.1016/S1369-7021(12)70163-3.

[40] ASTM International (2025) *ASTM E8/E8M-25: Standard Test Methods for Tension Testing of Metallic Materials*. West Conshohocken, PA: ASTM International. Available at: `https://compass.astm.org/content-access?contentCode=ASTM%7CE0008_E0008M-25%7Cen-US` (Accessed: 17 April 2026).

[41] K. Hussain, A. Tauqir, A. ul Haq, and A. Q. Khan, "Effect of retained austenite on gas nitriding of high strength steel," *Materials Science and Technology*, vol. 14, no. 12, pp. 1218–1220, Dec. 1998, doi: 10.1179/mst.1998.14.12.1218.

[42] E. A. Brandes and G. B. Brook, Eds., *Smithells Metals Reference Book*, 7th ed. Oxford: Elsevier, 2013.

[43] I. K. A. Widi, W. Sujana, and T. Rahardjo, "The Comparison of Nitrogen Atom Solubility in the Formation of Surface Layer on Stainless Steel and Alloy Steel," *Materials Science Forum*, vol. 1000, pp. 248–254, Jul. 2020, doi: 10.4028/www.scientific.net/MSF.1000.248.

[44] E. Roliński and G. Sharp, "Controlling Plasma Nitriding of Ferrous Alloys," *Materials Performance and Characterization*, vol. 6, no. 4, pp. 698–716, Oct. 2017, doi: 10.1520/MPC20160051.

[45] T. Lampe, S. Eisenberg, and G. Laudien, "Compound Layer Formation during Plasma Nitriding and Plasma Nitrocarburising," *Surface Engineering*, vol. 9, no. 1, Jan. 1993, doi: 10.1179/sur.1993.9.1.69.

[46] T. Peng, Y. Chen, X. Liu, M. Wu, Y. Lu, and J. Hu, "Phase constitution control of plasma nitrided layer and its effect on wear behavior under different loads," *Surface and Coatings Technology*, vol. 403, p. 126403, Dec. 2020, doi: 10.1016/j.surfcoat.2020.126403.

[47] S. Ojasalo, A. Antikainen, S. Nandy, V. Nurmi, M. Bojinov, V. Karastoyanov, and E. Huttunen-Saarivirta, "High-temperature corrosion of steels by nitridation in ammonia: Degradation mechanisms and comparison between steel grades," *Fuel*, vol. 419, p. 138872, Sep. 2026, doi: 10.1016/j.fuel.2026.138872.

[48] T. Zakroczymski, J. Flis, N. Lukomski, and J. Mankowski, "Entry, transport and absorption of hydrogen in low-temperature plasma nitrided austenitic stainless steel," *Acta Materialia*, vol. 49, no. 11, pp. 1929–1938, Jun. 2001, doi: 10.1016/S1359-6454(01)00112-4.

[49] J. A. Ronevich, J. G. Speer, G. Krauss, and D. K. Matlock, "Improvement of the Hydrogen Microprint Technique on AHSS Steels," *Metallography, Microstructure, and Analysis*, vol. 1, no. 2, pp. 79–84, Apr. 2012, doi: 10.1007/s13632-012-0015-y.

[50] Sandia National Laboratories, Technical Reference on Hydrogen Compatibility of Materials: Ferritic Stainless Steels (Code 1500), Technical Report, Sandia National Laboratories, 2021. Available at: `https://www.sandia.gov/app/uploads/sites/158/2021/12/1500TechRef_ferriticSS.pdf`

DEPARTMENT OF MECHANICAL ENGINEERING
CHALMERS UNIVERSITY OF TECHNOLOGY
Gothenburg, Sweden
www.chalmers.se



CHALMERS
UNIVERSITY OF TECHNOLOGY